UC Davis

UC Davis Previously Published Works

Title

Markov chain Monte Carlo inversion of mantle temperature and source composition, with application to Reykjanes Peninsula, Iceland

Permalink

https://escholarship.org/uc/item/060752z2

Authors

Brown, Eric L
Petersen, Kenni D
Lesher, Charles E

Publication Date

2020-02-01

DOI

10.1016/j.epsl.2019.116007

Peer reviewed

Markov chain Monte Carlo inversion of mantle temperature and source composition, with application to Reykjanes Peninsula, Iceland

Eric L. Brown [a],[*], Kenni D. Petersen [b], Charles E. Lesher [a],[c]

[a] *Dept. of Geoscience, Aarhus University, Denmark*
[b] *Aarhus GeoSoftware, Denmark*
[c] *Dept. of Earth and Planetary Sciences, University of California, Davis, USA*

ARTICLE INFO

ABSTRACT

The compositions and volumes of basalt generated by partial melting of the Earth's mantle provide fundamental constraints on the thermo-chemical conditions of the upper mantle. However, using melting products to interpret uniquely these conditions is challenging given the complexity of the melting and melt aggregation processes. Forward models simulating melting of lithologically heterogeneous mantle sources can account for this complexity, but require assumptions about key model input parameters, and the quality of the model fits to the observations are rarely, if at all, considered. Alternatively, inverse melting models can provide estimates of the quality of model fits to the observations, but as of yet, do not account for the presence of lithologic heterogeneity in the mantle source. To overcome these limitations, we present an inverse method coupling a Markov chain Monte Carlo (MCMC) sampling method with the REEBOX PRO forward mantle melting model. We use this tool to constrain mantle potential temperature, melt volumes, and the trace element and isotopic compositions of mantle source lithologies beneath the Reykjanes Peninsula of Iceland. We consider a range of plausible pyroxenite compositions (KG1, G2, and MIX1G) that span much of the range of natural pyroxenite compositions, and constrain the mantle potential temperature between 1455 and 1480 °C and pyroxenite abundance between 6.5 and 8.5%. These results are independent of the choice of pyroxenite composition and indicate that elevated potential temperatures and modest pyroxenite abundances are robust features of the Reykjanes Peninsula mantle source. The permitted ranges of pyroxenite trace element compositions vary as a function of pyroxenite fertility and mineralogy, but differ from the compositions of subduction-modified recycled oceanic crust typically used in previous models, indicating a more complex petrogenetic origin for the pyroxenite source than previously considered. As all of the pyroxenites employed here yield equally good fits to the geochemical and geophysical observations along the Reykjanes Peninsula, forward models should not be used to constrain the major element character of pyroxenite present in mantle source regions based solely on the trace element/isotopic compositions (and volumes) of basalts. Given the range of lithologies included in REEBOX PRO and the flexibility of MCMC inversion, this method may be applied to constrain thermal and compositional source characteristics in a wide variety of basalt source regions.

1. Introduction

It has long been appreciated that oceanic basalts are derived from thermally and compositionally heterogeneous mantle domains (e.g., Gast et al., 1964; Cawthorn, 1975; Klein and Langmuir, 1987). Thus, to gain better insight into the long-term and ongoing thermal and chemical evolution of the Earth, geochemists and petrologists often use the compositions and volumes of mantle-derived basalts to constrain mantle potential temperature (T_P) and the abundances (Φ) and compositions (X) of the lithologies comprising basalt mantle source regions (e.g., Brown and Lesher, 2014; Klein and Langmuir, 1987; Matthews et al., 2016; Putirka et al., 2007; Shorttle et al., 2014). Using basalts to constrain uniquely these factors is challenging given the filter between the solid mantle source and the erupted basalt imposed by the melting process itself. Seeing through this process to relate basalt compositions and volumes reliably to thermochemical and dynamical conditions in their source regions requires accounting for the melting behaviors of multiple lithologies (e.g. peridotite vs. pyroxenite), segregation efficiency of near-fractional melts derived from these lithologies

over ranges of pressure and temperature, and their eventual mixing and differentiation in transit to Earth's surface.

In recent years a number of forward models accounting for these intricacies have been developed to better constrain aspects of the mantle source conditions and melting process beneath Iceland. Some of these models have focused on constraining T_P and/or the abundance of pyroxenite (Φ_{px}) comprising the Iceland source using geochemical and/or geophysical observations (Sobolev et al., 2007; Brown and Lesher, 2014; Shorttle et al., 2014; Lambart et al., 2016; Matthews et al., 2016). In these models however, the trace element/isotopic compositions of the source lithologies were assumed a priori (Brown and Lesher, 2014), or were not considered at all. Conversely, some have focused on modeling observed Iceland basalt compositions to constrain either melt mixing processes (Stracke and Bourdon, 2009; Koornneef et al., 2012a; Rudge et al., 2013), or the melting behavior of the pyroxenite source lithology (Lambart, 2017). However, these applications assumed values for T_P (or the depth of the onset of melting), Φ_{px}, and the initial trace element/isotopic compositions of the model peridotite and pyroxenite sources a priori. Thus, the quality of the constraints on T_P and Φ_{px} obtained in these forward models are difficult to assess. Furthermore, constraints on the trace element and isotopic compositions of the sources are lacking because they have not been explored systematically by these models.

Here we present a new and versatile method combining Markov chain Monte Carlo (MCMC) sampling with the forward melting model REEBOX PRO (Brown and Lesher, 2016) to invert for mantle source characteristics governing basaltic magmatism. This method simulates melting of lithologically heterogeneous mantle and places simultaneous and quantitative constraints on T_P, Φ, and the trace element and isotopic compositions of end-member source lithologies. A significant advantage of the approach is that it does not require a priori assumptions about the values of these key parameters, as they are determined from minimizing model misfits to the observations. To illustrate our approach to mantle melting problems we consider magmatism along the Reykjanes Peninsula, Iceland that is well characterized in terms of petrology, geochemistry, and geophysics. Here, we constrain the thermochemical conditions (and their uncertainties) for the Reykjanes Peninsula mantle source by inverting for REEBOX PRO inputs that generate outputs matching both geochemical and geophysical observations. Our modeling is the first to determine T_P, Φ, and X simultaneously for mantle melting beneath Iceland, demonstrating the utility of our modeling approach. The flexibility of both MCMC sampling and REEBOX PRO make this method broadly applicable to a variety of tectonomagmatic settings.

2. The tools: Markov chain Monte Carlo inversion and REEBOX PRO

2.1. General background

To gain better insight into the thermal and compositional state of the mantle, we seek quantitative constraints on T_P, Φ, and X of basalt mantle source regions. We developed the mantle melting model REEBOX PRO (Brown and Lesher, 2016) using these parameters as inputs to provide such constraints by forward modeling basalt compositions and volumes (e.g., Brown and Lesher, 2014). However, determining the optimal combination of these inputs (and their uncertainties) is not easily achieved by forward modeling given the potentially large number of parameters involved (including up to 24 trace elements and 4 isotopes for *each* lithology). Furthermore, how well outputs from such models fit the observations (and thus, how well the model input parameters constrain the observations) is rarely quantified in forward modeling

applications. In this regard, inverse modeling methods are appealing because they systematically vary the model parameters of interest to minimize misfits between model outputs and observations and estimate parameter uncertainties. Unfortunately, existing inverse mantle melting models (including the INVMEL model of McKenzie and O'Nions, 1991) are of limited applicability to lithologically heterogeneous sources because they all assume melting of a homogeneous peridotite source (e.g., Allegre and Minster, 1978; Hofmann and Feigenson, 1983; Liu and Liang, 2017; McKenzie and O'Nions, 1991; Minster and Allegre, 1978).

2.2. Inversion background

To overcome the noted difficulties in forward modeling and the limitations of existing inverse models to homogeneous peridotite sources, we have developed a method to invert for these key REEBOX PRO model parameters (T_P, Φ, X) and their associated uncertainties. Following Tarantola (2005), the probability that a given set of model parameters (**m**) explains a given set of observations (data; **d**) can be described as

$$\rho(\mathbf{m}, \mathbf{d}) = kq(\mathbf{m})L(\mathbf{d}, \mathbf{m}), \qquad (1)$$

where k is a normalization constant, $q(\mathbf{m})$ is the *prior probability distribution*, $L(\mathbf{d}, \mathbf{m})$ is the data *likelihood* function, and $\rho(\mathbf{m}, \mathbf{d})$ is the *posterior probability distribution* (in other works (e.g. Gallagher et al., 2009) the *posterior probability distribution* and data *likelihood* function are written as $\rho(\mathbf{m} \mid \mathbf{d})$ and $L(\mathbf{d} \mid \mathbf{m})$, respectively).

The *prior probability distribution* ($q(\mathbf{m})$) describes what is known about the **m** model parameters a priori and is independent of observations. This information includes the range and distribution (e.g. normal or uniform) of values for each model parameter, and any additional model constraints. For example, in the present application we assume a uniform distribution of model parameter values between generous bounds and require that the mantle source undergoing melting is sufficiently buoyant to upwell for all combinations of T_P and Φ_{px} (see below). The data *likelihood* ($L(\mathbf{d}, \mathbf{m})$) is a measure of how well the resulting model outputs fit the observations (often quantified as the sum of the least squares misfits between model outputs and data). Finally, the *posterior probability distribution* ($\rho(\mathbf{m}, \mathbf{d})$) describes the distribution of all model parameter values contained in $q(\mathbf{m})$ that produce models matching the observations (as quantified by $L(\mathbf{d}, \mathbf{m})$).

Although Eq. (1) provides an explicit description of the *posterior probability distribution*, the normalization constant k is generally unknown. Because an infinite number of model parameters is theoretically possible, a method of sampling $\rho(\mathbf{m}, \mathbf{d})$ is needed. Markov chain Monte Carlo (MCMC) methods provide such sampling by generating a sequence of randomly generated models (Markov chain) whose **m** have a combined distribution that approximates $\rho(\mathbf{m}, \mathbf{d})$ (Gilks et al., 1996). In this context a "model" is a single forward calculation (and its resulting outputs) based on a set of model inputs, **m**. Here we use the Metropolis algorithm (Metropolis et al., 1953) to construct a Markov chain. The algorithm consists of the following steps (we provide a worked example of the algorithm from our Reykjanes Peninsula case study in the *Supplementary Information*).

- *Step 1. Markov chain initiation*. An initial set of model input parameters, **m**, are randomly drawn from the *prior probability distribution*, $q(\mathbf{m})$. To be valid, these **m** must not violate any prior constraints. The values contained in **m** constitute the first entry in the Markov chain and are taken as "current". Using an iteration variable, t, the "current" parameters are written as $\mathbf{m_t}$, where here $t = 1$. A forward model calculation is made using $\mathbf{m_t}$, and the resulting model fit to the observations is quantified using the *likelihood* function [$L(\mathbf{d}, \mathbf{m_t})$].

- *Step 2. Model parameter proposal*. A new set of model parameters ($\mathbf{m_{t'}}$) is proposed by randomly perturbing the "current" parameters ($\mathbf{m_t}$). A forward model calculation is made using $\mathbf{m_{t'}}$, and the resulting model fit to the observations is quantified using the *likelihood* function [$L(\mathbf{d}, \mathbf{m_{t'}})$].
- *Step 3. Proposed model parameter acceptance or rejection.*
  - *Part A. Calculate the "acceptance" ratio*. To determine whether $\mathbf{m_{t'}}$ is accepted into the Markov chain (or rejected and discarded), the Metropolis algorithm first calculates an "acceptance" ratio, R. This is the ratio of the *posterior probabilities* of the models calculated using the proposed and "current" model parameters

$$R = \frac{\rho(\mathbf{m_{t'}}, \mathbf{d})}{\rho(\mathbf{m_t}, \mathbf{d})} = \frac{k\, q(\mathbf{m_{t'}}) L(\mathbf{d}, \mathbf{m_{t'}})}{k\, q(\mathbf{m_t}) L(\mathbf{d}, \mathbf{m_t})} = \frac{q(\mathbf{m_{t'}}) L(\mathbf{d}, \mathbf{m_{t'}})}{q(\mathbf{m_t}) L(\mathbf{d}, \mathbf{m_t})}. \quad (2)$$

The normalization constant, k, cancels in Eq. (2) and thus does not need to be known. Furthermore, assuming no parameters in $\mathbf{m_{t'}}$ violate prior constraints, $q(\mathbf{m_t}) = q(\mathbf{m_{t'}}) = constant$ because we assume a uniform distribution for each parameter in $q(\mathbf{m})$. Thus, these terms also cancel in Eq. (2) and R reduces to the ratio of the proposed and "current" *likelihoods*. However, it is possible that $\mathbf{m_{t'}}$ does violate some prior constraint(s)- in such cases $q(\mathbf{m_{t'}}) = 0$, leading to $\rho(\mathbf{m_{t'}}, \mathbf{d}) = 0$.

  - *Part B. Draw a random number to compare to R*. A random number, r, is drawn from a uniform distribution between 0 and 1. If $r \leq R$, then $\mathbf{m_{t'}}$ is accepted and added to the Markov chain, and the proposed parameters become "current" (i.e., $\mathbf{m_{t'}} = \mathbf{m_{t+1}}$). However, if $r > R$, then the proposed parameters are rejected and discarded, and the "current" parameters remain "current" (i.e., are accepted again; $\mathbf{m_t} = \mathbf{m_{t+1}}$). The iteration variable t is incremented; $t = t+1$ (where $t = 2$ in this case).
- *Step 4. Repeat Steps 2 and 3 until a specified number of iterations have been made*. In the application presented below, we ran 200,000 iterations.

The Metropolis acceptance criteria that $r \leq R$ has several important implications. Firstly, because $r \leq 1$, $\mathbf{m_{t'}}$ is *always* accepted if it yields a higher *posterior probability* than $\mathbf{m_t}$ (since $R > 1$). Secondly, if $\mathbf{m_{t'}}$ violates a prior constraint, then $R = 0$. In practice, such $\mathbf{m_{t'}}$ are rejected since there is an infinitesimally small chance that $r = 0$. Finally, $\mathbf{m_{t'}}$ resulting in a lower *posterior probability* than $\mathbf{m_t}$ (i.e., $R < 1$) may still be accepted, as the ability to accept less probable $\mathbf{m_{t'}}$ allows for the statistical sampling of parameter space around the region of highest *likelihood*.

Since the initial $\mathbf{m_t}$ is drawn at random from $q(\mathbf{m})$, a good fit to the data is not guaranteed for the first many $\mathbf{m_t}$ in the chain. However, since the Metropolis procedure always accepts $\mathbf{m_{t'}}$ with higher probability, $\rho(\mathbf{m_t}, \mathbf{d})$ typically increases rapidly in the beginning of the Markov chain (often called "burn-in" of the chain). Beyond the point of "burn-in", the random walk through parameter space effectively samples a range of parameter values that are all generally probable. The collection of these post-"burn-in" $\mathbf{m_t}$ is thus assumed to have a distribution approximating $\rho(\mathbf{m}, \mathbf{d})$ (Gallagher et al., 2009), allowing us to use the combined distribution of the post-"burn-in" $\mathbf{m_t}$ to identify the most probable parameter values and their uncertainties that explain the observations. See the *Supplementary Information* for further details.

2.3. REEBOX PRO

The REEBOX PRO melting model (Brown and Lesher, 2016) simulates adiabatic decompression melting of pyroxenite-bearing peridotite sources. In addition to the G2 and MIX1G pyroxenites included in the initial REEBOX PRO release, we have now added a
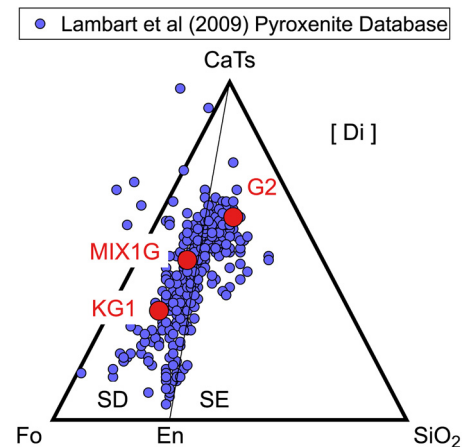

Fig. 1. Range of natural pyroxenite compositions (from Lambart et al., 2009) plotted within the projection scheme of O'Hara (1968). The three model pyroxenite compositions included in REEBOX PRO shown in red span much of the range of the natural pyroxenites. SD = silica deficient pyroxenite; SE = silica excess pyroxenite. Fo = forsterite, CaTs = calcium Tschermak, En = enstatite, and Di = diopside. The three pyroxenites used in this study noted in red (G2, MIX1G, and KG1) span much of the range of the natural pyroxenites. (For interpretation of the colors in the figure(s), the reader is referred to the web version of this article.)

KG1 pyroxenite (Kogiso et al., 1998) melting parameterization (described in Appendix A). As shown in Fig. 1, the addition of KG1 pyroxenite is an enhancement that significantly expands the compositional range covered by the program for potential pyroxenite lithologies within the convecting mantle.

REEBOX PRO assumes that coexisting source lithologies remain in thermal equilibrium and quantifies the extent of melting for each individual lithology along a given decompression melting path using experimentally-constrained melting functions and thermodynamic expressions for isentropic polybaric melting. Instantaneous melt compositions generated along the decompression melting path are calculated assuming non-modal incremental batch melting. As a forward modeling tool, REEBOX PRO requires the user to input T_P, and make choices about source compositions in terms of the relative abundances of the peridotite and pyroxenite lithologies (Φ), and their trace element and isotopic compositions (X).

Currently, REEBOX PRO can model up to four radiogenic isotope systems and 24 incompatible trace elements, with default and user-defined options for mineral-liquid elemental partition coefficients. The program outputs trace element and isotopic compositions of a) all instantaneous incremental batch melts generated by each lithology for every 0.01 GPa along the melting path, b) all instantaneous melts accumulated along the decompression melting path for each lithology (column-accumulated melts), and c) the bulk (aggregate) igneous crust (and its thickness) formed by pooling all instantaneous melts from all melting lithologies (pooled melts). Finally, care must be taken to ensure that model results are compared with fractionation-corrected basalt compositions, and/or ratios of similarly incompatible elements and radiogenic isotopes unaffected by crystallization because REEBOX PRO predicts primary magma compositions unaffected by crystallization. Additional background, benchmarks and example applications of REEBOX PRO are provided by Brown and Lesher (2016) and the latest version (1.1) including the addition of KG1 pyroxenite can be downloaded from http://geo.au.dk/forskning/forskningscentre/earth-system-petrology/reebox-pro.

3. MCMC implementation for the Reykjanes Peninsula, Iceland

In the following sections, we describe our Metropolis MCMC implementation to invert for mantle source characteristics beneath
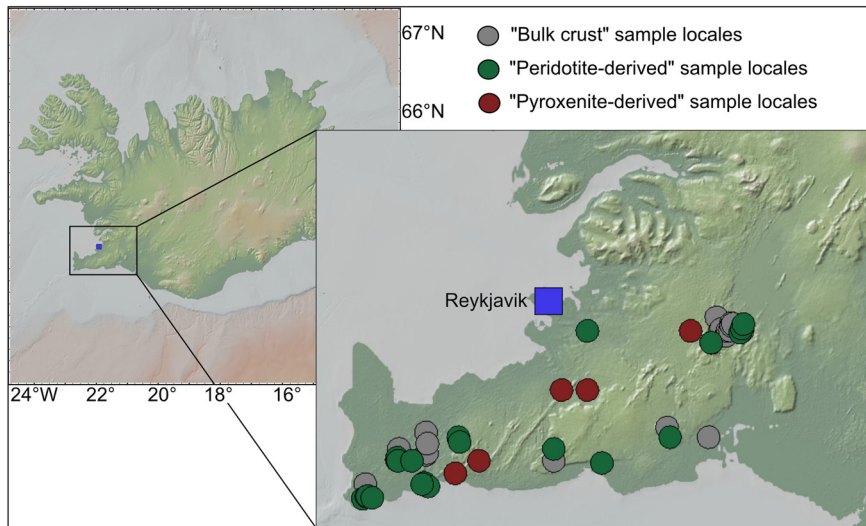
Fig. 2. Location map of Iceland with inset showing sample locations used in this study (made using GeoMapApp; http://www.geomapapp.org). Grey circles denote sample locales containing basalts representative of the "bulk crust" composition. Green and red circles denote sample locales for the "peridotite-derived" and "pyroxenite-derived" basalts, respectively. All samples taken from the pre-compiled October 2017 Iceland dataset from GEOROC; http://georoc.mpch-mainz.gwdg.de. See text for further details about the different basalt suites.

the Reykjanes Peninsula. We first describe the observational constraints from Reykjanes Peninsula used in the inversion, and then detail how they are employed in equation (1). The model parameters we wish to invert and their *prior probability distribution* are then described, followed by some final details of our implementation.

3.1. Geophysical and geochemical observations

The Reykjanes Peninsula of southwest Iceland (Fig. 2) is the on-land extension of Reykjanes Ridge, and is underlain by 16-20 km thick igneous crust (Darbyshire et al., 2000). Reykjanes Peninsula lavas consist primarily of primitive to evolved olivine tholeiites bounded by chemically and isotopically depleted (e.g. Nb/Zr $\sim$ 0.04; ^{143}Nd/^{144}Nd $\geq$ 0.513070) and enriched (Nb/Zr $\sim$ 0.15; ^{143}Nd/^{144}Nd $\sim$ 0.513001) end-member compositions (Gee et al., 1998). These end-member melt compositions are not related by fractional crystallization but are thought to represent melt compositions derived from peridotite and pyroxenite domains, respectively, in the Iceland mantle source (Shorttle and Maclennan, 2011). As shown in Fig. 3, many lavas have Nb/Zr intermediate to the low and high Nb/Zr of the end-members, and the range and variability of Nb/Zr at any given MgO content diminishes with decreasing MgO. These systematics are well explained by a process of concurrent mixing and crystallization (Gee et al., 1998; Shorttle and Maclennan, 2011) – progressive mixing of peridotite and pyroxenite-derived melts coupled with fractional crystallization (that drives down the MgO content) yields evolved lavas with Nb/Zr intermediate to the end-members. An important consequence of this process is that ratios of similarly incompatible elements and radiogenic isotopic compositions of the most evolved basalt compositions (<6 wt.% MgO) are representative of the bulk igneous crust composition (Maclennan, 2008b; Shorttle et al., 2014).

The chemical distinctions between the end-member peridotite- and pyroxenite-derived melts and the evolved basalts representative of the bulk crust indicate that the different basalt suites result from different styles of melt accumulation from the heterogeneous source. For example, the chemically distinct primitive peridotite- and pyroxenite-derived basalt compositions indicate they did not mix with each other prior to eruption. Using olivine-hosted melt inclusions, Maclennan (2008a, 2008b) argued

that a bimodal distribution of depleted and enriched melt compositions (e.g., peridotite- and pyroxenite-derived melts) are supplied to the Iceland crust by porous flow in the mantle. These end-member melts represent mixtures of instantaneous melts sampled along the center and edges of the mantle melting column, respectively. However, the proportion of the melting column over which they are aggregated remains an open question (Gurenko and Chaussidon, 1995; Neave et al., 2018). Likewise, average crustal thickness is proportional to the total volume of melt generated in the corner-flow regime, while the compositions of the most evolved basalts are the product of mixing and differentiation in crustal-level magma chambers (e.g. Shorttle et al., 2014).

It is the goal of our modeling to constrain T_P, Φ, X of the peridotite and pyroxenite sources beneath the Reykjanes Peninsula by finding models that best match the compositions of a) the primitive peridotite-derived basalts, b) the primitive pyroxenite-derived basalts, and c) the mean bulk crust composition and thickness as exemplified by the most evolved basalts. We do not model those lavas with compositions intermediate to the end-member peridotite- and pyroxenite-derived basalts and the most evolved (bulk crust-like) lavas because they result from stochastic mixing processes in the crust better described by statistical modeling (Shorttle et al., 2016). This contrasts with previous efforts (Koornneef et al., 2012a; Lambart, 2017; Stracke and Bourdon, 2009) that attempted to fit model melt curves through correlations of radiogenic isotopes/incompatible trace element ratios of *all* samples.

3.2. Likelihood function $L(\mathbf{d}, \mathbf{m})$

We calculate a single value that describes the overall quality of how well the REEBOX PRO model outputs ($\boldsymbol{\mu}$) fit the Reykjanes Peninsula observations (data; $\mathbf{d}$) within the observational uncertainties ($\boldsymbol{\sigma}$) among N model and data values

$$L(\mathbf{d}, \mathbf{m}) = \Pi_{i=1}^{N} \frac{1}{\sqrt{2\pi}\sigma_i} \exp\left(-\frac{(d_i - \mu_i)^n}{2\sigma_i^n}\right). \quad (3)$$

In our formulation, the comparison between model outputs and data is quantified as a least squares misfit (i.e., the exponential factor $n = 2$) for all parameters except igneous crustal thickness, where $n = 20$ (see below) (in practice, we quantify the log of
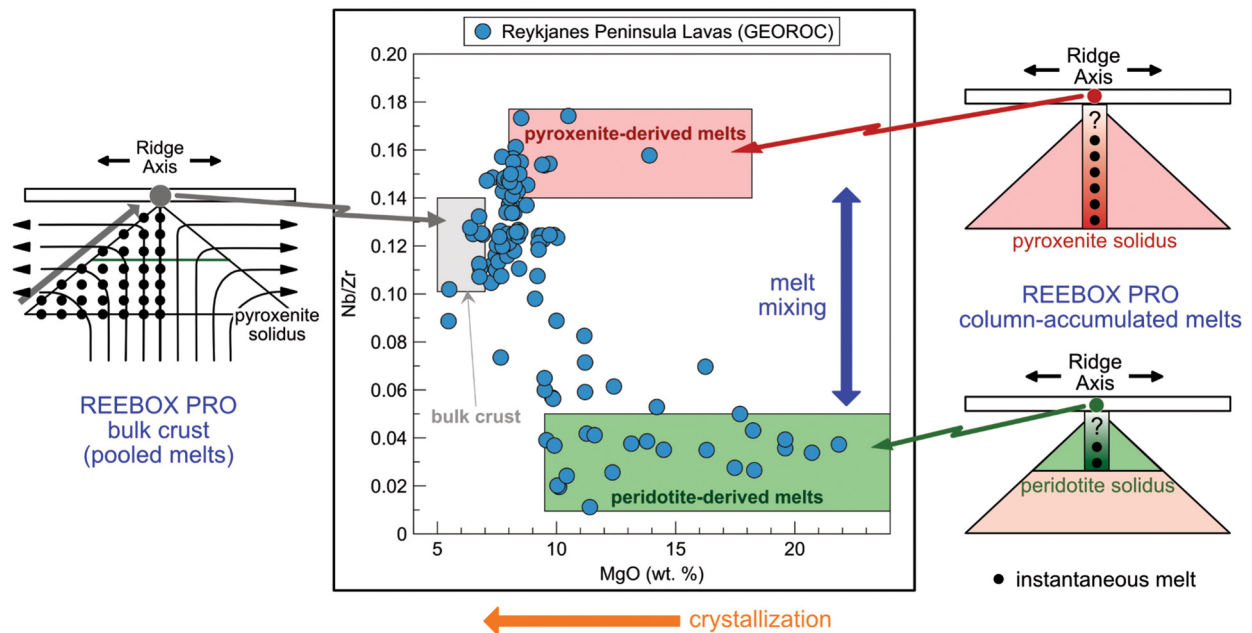
Fig. 3. Nb/Zr vs. MgO for Reykjanes Peninsula data used in this study (pre-compiled October 2017 Iceland dataset from GEOROC; http://georoc.mpch-mainz.gwdg.de). Primitive lavas with low Nb/Zr and high Nb/Zr are derived from peridotite (green box) and pyroxenite (red box) sources, respectively (Shorttle and Maclennan, 2011). Concurrent mixing (blue arrow) and crystallization (orange arrow) serve to homogenize the end-member melt compositions, such that lavas with lower MgO are aggregated melts with a composition similar to the bulk igneous crust (grey box) (Maclennan, 2008b; Shorttle et al., 2014). Sample locations are given in Fig. 2. Also shown are schematic, 2-D cross-sections through the hypothetical melting zone showing the types of calculations from REEBOX PRO (Brown and Lesher, 2016) used to model the different aspects of the geochemical observations. Primitive end-member peridotite- and pyroxenite-derived melts are modeled using the column-accumulated melt compositions from REEBOX PRO (i.e., instantaneous melts are accumulated along the melting column beneath the ridge axis). Given uncertainty in the length of the melting column over which the instantaneous melts are accumulated, we leave this as a free parameter that is included in the inversion. The evolved lavas representative of the bulk crust are modelled using the bulk igneous crust composition output by REEBOX PRO, which is quantified by pooling all instantaneous melts from both the peridotite and pyroxenite lithologies, in the proportions they were formed. Additional details are provided by Brown and Lesher (2016) and in the text.

$L(\mathbf{d}, \mathbf{m})$ for computational stability). The specific observations ($\mathbf{d}$), their uncertainties (σ), and the specific model outputs (μ) used in the inversion are described next.

3.2.1. Observational components of $L(\mathbf{d}, \mathbf{m})$

For the data component of the *likelihood* function ($\mathbf{d}$ and σ), we utilize the October 2017 pre-compiled Iceland data set from GEOROC (http://georoc.mpch-mainz.gwdg.de/georoc/), which we filtered to only include extrusive samples with ≥ 5 wt.% MgO located between 63.8-64.1°N and 21.09-23°W (i.e., the Reykjanes Peninsula; Fig. 2). Within the Reykjanes Peninsula dataset (Fig. 3), we identify plausible primitive peridotite-derived melts as those with MgO ≥ 9.5 wt.% and Nb/Zr ≤ 0.05 and plausible pyroxenite-derived melts as those with MgO ≥ 8 wt.% and Nb/Zr ≥ 0.14 (Shorttle and Maclennan, 2011; Shorttle et al., 2014). Evolved lava compositions representative of the mean bulk igneous crust composition are those with 5-7 wt.% MgO (Shorttle and Maclennan, 2011; Shorttle et al., 2014).

As the primitive peridotite- and pyroxenite-derived melts are dominated by olivine fractionation (Gee et al., 1998), we account for these effects (Appendix B) to facilitate direct comparison between the absolute elemental abundances in these suites and the primary magma compositions output by REEBOX PRO. We thus utilize the mean and one standard deviation of the mean (S.D.) of the fractionation-corrected concentrations of 22 incompatible trace elements (Rb, Ba, Th, U, Nb, Ta, K, La, Ce, Pb, Pr, Nd, Sm, Zr, Hf, Ti, Gd, Dy, Y, Er, Yb, Lu) and the ^{143}Nd/^{144}Nd and ^{206}Pb/^{204}Pb compositions for these corrected peridotite- and pyroxenite-derived basalts in $L(\mathbf{d}, \mathbf{m})$. Also included in $L(\mathbf{d}, \mathbf{m})$ are the mean and 1 S.D. of ratios of neighboring elements on the multi-element diagram (Rb/Ba, Ba/Th, Th/U, U/Nb, Nb/Ta, Ta/K, K/La, La/Ce, Ce/Pb, Pb/Pr, Nd/Sm, Sm/Zr, Zr/Hf, Ti/Gd, Gd/Dy, Dy/Y, Y/Er, Er/Yb, Yb/Lu, and Nb/Zr) for both the peridotite- and pyroxenite-derived suites to ensure

that the relative enrichments and depletions (relative to neighboring elements) on multi-element diagrams are also captured by the models. All elemental and ratio uncertainties in $L(\mathbf{d}, \mathbf{m})$ are assumed to be normally distributed.

In contrast, the absolute elemental concentrations for the most evolved basalts representative of the bulk crust cannot be utilized in $L(\mathbf{d}, \mathbf{m})$ because they have been influenced by extensive fractionation of wehrlite and gabbro (Maclennan et al., 2001). Thus, the likelihood function includes the mean and 1 S.D. of the mean for ^{143}Nd/^{144}Nd and ^{206}Pb/^{204}Pb and 72 incompatible trace element *ratios* from these evolved basalts that are little affected by gabbro and wehrlite crystallization (Appendix C). As above, we assume normal distributions for the uncertainties on these ratios.

Finally, $L(\mathbf{d}, \mathbf{m})$ also includes the bulk crustal thickness constrained by geophysics (Darbyshire et al., 2000). However, it is difficult to ascribe a single value for the crustal thickness given the observed range (16-20 km; Darbyshire et al., 2000). We therefore assume an approximately uniform distribution (i.e., $n = 20$ in equation (2)), with a mean value of 18 km $\pm$ 1.5 km (the average of the range of crustal thickness estimates when accounting for ± 1 km uncertainty in these geophysical estimates). Altogether, 163 comparisons between model outputs and observations are included in $L(\mathbf{d}, \mathbf{m})$. All data means (and their associated 1 S.D.) used in $L(\mathbf{d}, \mathbf{m})$ are provided in *Supplementary Table 1*, and the raw data, as well as all fractionation-corrected compositions used in the modeling, are provided in an Excel workbook entitled *Geochemical Database* in the *Supplementary Information*.

3.2.2. Model components of $L(\mathbf{d}, \mathbf{m})$

Given the geochemical systematics and melt accumulation processes noted above, the end-member peridotite- and pyroxenite-derived basalt compositions are best represented by the peridotite and pyroxenite column-accumulated melt compositions, respec-

tively, output by REEBOX PRO. However, given the uncertainty about the length of the melting column over which the instantaneous melts are accumulated, we allow the tops of the melting columns from which the instantaneous peridotite and pyroxenite melts are accumulated to be free parameters in the MCMC simulations. The bulk crust composition and thickness constrained by the evolved basalt compositions and geophysics, respectively, are best represented by the modelled bulk igneous crust composition and thickness derived by pooling all instantaneous melts from all lithologies over a triangular melting zone (e.g. Shorttle et al., 2014). The REEBOX PRO modeling scenarios for the different basalt suites are illustrated in Fig. 3.

3.3. Model input parameters: prior probability distribution, $q(\mathbf{m})$

To constrain mantle source conditions beneath the Reykjanes Peninsula we invert for the values (and uncertainties) of the following REEBOX PRO inputs: T_P, the initial mass fractions of the (anhydrous) peridotite and pyroxenite source lithologies ($\Phi_{per} + \Phi_{px} = 1$), and the concentrations of 22 incompatible trace elements (Rb, Ba, Th, U, Nb, Ta, K, La, Ce, Pb, Pr, Nd, Sm, Zr, Hf, Ti, Gd, Dy, Y, Er, Yb, and Lu), and $^{143}Nd/^{144}Nd$ and $^{206}Pb/^{204}Pb$ compositions for both source lithologies. As noted above, we also invert for the lengths of the melting column over which the instantaneous peridotite and pyroxenite melts are accumulated to yield the end-member peridotite- and pyroxenite-derived basalts. In total, we invert for 52 model parameters (we only invert for Φ_{px}, deriving Φ_{per} from mass balance).

For the *prior probability distribution*, we take the conservative approach and assume that each of these model parameters is uniformly distributed between some upper and lower bounds. To ensure a sufficient range of model parameter space to explore, we chose bounds on the trace element and isotopic compositions that greatly exceed those used in previous forward modeling at Iceland (Koornneef et al., 2012a; Lambart, 2017; Rudge et al., 2013; Stracke and Bourdon, 2009; Brown and Lesher, 2014). For example, the peridotite source trace element abundances range from 1/16th the concentrations in depleted MORB mantle (DMM; Salters and Stracke, 2004; Workman and Hart, 2005) to concentrations that are up to four times those of DMM. For the pyroxenite source, the trace element abundances range from DMM to five times the concentration of enriched MORB (Gale et al., 2013). We also consider a range of potential temperatures that span ambient mantle T_P (1330 °C) up to 1570 °C, which is ∼50-100 °C higher than the T_P previously inferred or assumed for the mantle beneath Iceland (Sobolev et al., 2007; Rudge et al., 2013; Brown and Lesher, 2014; Shorttle et al., 2014; Lambart, 2017).

Although olivine-bearing KG1 pyroxenite is thought to be a suitably enriched source lithology for Iceland (Lambart, 2017; Neave et al., 2018; Shorttle and Maclennan, 2011), our approach relaxes this constraint as REEBOX PRO also includes the melting behavior of G2 and MIX1G pyroxenite. Drawing on our previous work (Brown and Lesher, 2014), we specify that the maximum amount of pyroxenite permitted in the source is limited by the condition of neutral buoyancy for a given T_P. For example, for $T_P = 1570$ °C, the neutral buoyancy condition is met for Φ_{px} of 0.27 for KG1, 0.21 for G2 and 0.18 for MIX1G pyroxenite. If any proposed combination of T_P and Φ_{px} is too dense to upwell, then $q(\mathbf{m}) = 0$. Finally, the proportions of the peridotite and pyroxenite melting columns over which instantaneous melts are accumulated to form the model end-member peridotite- and pyroxenite-derived magmas are allowed to range from 0.01 (i.e., the base of the melting column) to 1 (the top of the melting column). As we show in Appendix D for the Reykjanes Peninsula, in all models instantaneous melts for both source lithologies are accumulated over most of their respective melting columns.
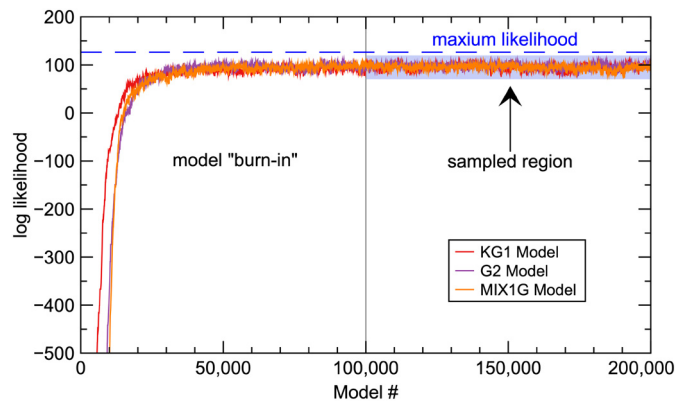

Fig. 4. MCMC log likelihood (measure of the goodness of the model fit to the data) as a function of model run for Markov chains involving KG1 (red curve), G2 (purple curve), and MIX1G (orange curve) pyroxenites. Maximum log likelihood (i.e., perfect fit of model to observations) is shown as blue-dashed line. The first 100,000 models are considered model "burn-in", whereas the last 100,000 models in each chain are used to sample the *posterior probability density distribution*, as illustrated by the blue band. Figs. 4–7 are generated from these 100,000 samples of the *posterior probability density*.

The bounds of the model parameters in $q(\mathbf{m})$ are given in *Supplementary Table 2*. For tractability, we assume in this work passive upwelling, but acknowledge there may be a component of active upwelling beneath the Reykjanes Peninsula (Koornneef et al., 2012b; Brown and Lesher, 2014). The present model does not include this possibility, but it could be considered in the future by adding the U-series isotopes to REEBOX PRO to place additional geochemical constraints on upwelling rate. Finally, we assume default values for all model parameters required to run REEBOX PRO that are not included in the inversion, including the appropriate mineral-liquid partition coefficients.

3.4. Final details

To ensure that a sufficient number of models sample the *posterior probability distribution*, we set each Markov chain to terminate after 200,000 model proposals. As identifying when model burn-in has been achieved is difficult and somewhat subjective, we use the last 100,000 models in each chain to represent $\rho(\mathbf{m}, \mathbf{d})$ (termed "burned-in models" hereafter; Fig. 4). To ensure that these highest likelihood samples are representative of $\rho(\mathbf{m}, \mathbf{d})$ and represent global maxima instead of local maxima in the model parameter space, we ran five different Markov chains with different, randomized initial starting parameters for each of the three pyroxenite lithologies considered (i.e., 15 Markov chains in total). For a given pyroxenite lithology, each of the five different chains yields similar $\rho(\mathbf{m}, \mathbf{d})$ (shown in the *Supplementary Information*), showing that the sampling procedure is indeed robust. To simplify the presentation below, we present and discuss the results from single representative Markov chains for models employing each of the three pyroxenite lithologies (termed the KG1, G2, and MIX1G chains, respectively).

4. Model results for the Reykjanes Peninsula

4.1. Model fits to Reykjanes Peninsula observations

Figs. 5–6 summarize the burned-in (posterior) REEBOX PRO model fits to the observations used in the *likelihood* function. In Fig. 5, mean model pooled melt compositions (and their associated 1 S.D.) are normalized by their corresponding bulk crust mean values. As can be seen, in most cases the model mean values are within their 1 S.D. of the mean bulk crust values (i.e., they fall near the line at unity), and in all cases, the model mean
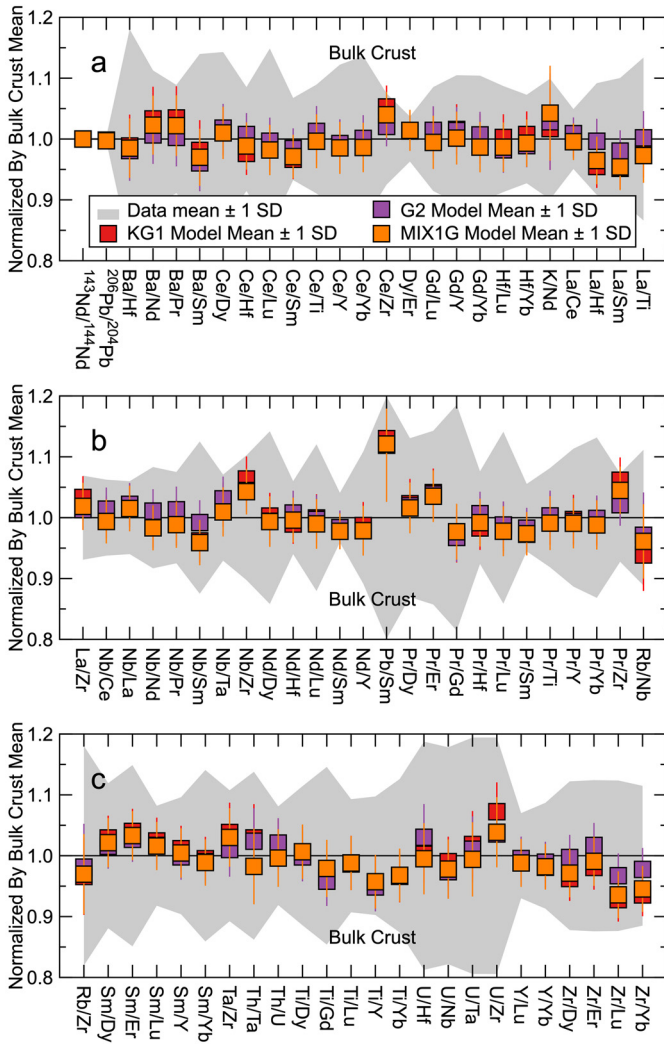
Fig. 5. Panels **a-c** show posterior bulk crust ratios from the MCMC inversion (mean and 1 standard deviation (S.D.) of mean from 100,000 posterior models for each of the 3 pyroxenite Markov chains; colors for each pyroxenite chain as in Fig. 3) normalized by the mean values of the bulk crust (observations). All model means (and their 1 S.D.) fall within the 1 S.D. uncertainties of the observations (grey fields), indicating good model fits to the bulk crust observations.

values are within the 1 S.D. of the observations (grey fields in Fig. 5). Although more variable, posterior model fits to the primary peridotite- and pyroxenite-derived magma compositions from the KG1, G2, and MIX1G chains are within the 1 S.D. uncertainties of the magma compositions for all observables (Fig. 6).

Fig. 7 shows the distributions of posterior model igneous crustal thicknesses for each of the three different chains. Median model crustal thicknesses range from 18.8-19.4 km, within the range of crustal thickness estimates for the area. Taken together, these results indicate that the high likelihood values achieved by each of the three different chains (Fig. 4) result from fitting all geochemical and geophysical observations within their uncertainties.

4.2. Posterior distributions of model parameters, $\rho(\mathbf{m}, \mathbf{d})$

The key REEBOX PRO model parameters sampled from the *posterior probability density* for the KG1, G2, and MIX1G pyroxenite chains are shown in Figs. 8–10 (and summarized in *Supplementary Table 3*). Histograms of posterior T_P and Φ_{px} are shown in Fig. 8a-b, respectively, where the median T_P and Φ_{px} range from 1454-1482 °C and 0.065-0.084, respectively. G2 pyroxenite yields a lower median T_P and Φ_{px} (1454 °C and 0.065, respectively) than

KG1 or MIX1G (T_P = 1476-1482 °C; Φ_{px} = 0.082-0.084). Nevertheless, in all cases, 50% of the models (defined as those between the lower and upper quartiles) fall within ~3-6 °C and ~0.004-0.007 of their median T_P and Φ_{px}, respectively (corresponding to standard deviations of 5.6-9 °C and 0.007-0.009, respectively; *Supplementary Table 3*).

Fig. 9 shows a primitive mantle-normalized multi-element diagram summarizing the mean trace element compositions (and their associated 1 S.D.) of the model peridotite and pyroxenite sources for the KG1, G2, and MIX1G chains. Here, it can be appreciated that the model peridotite sources in the three different chains have posterior compositions that are within their 1 S.D. uncertainties of each other for most elements. In contrast, the posterior trace element abundances of the model pyroxenite sources from the different chains exhibit key differences from each other. Although the posterior trace element abundances of the three model pyroxenite sources are generally similar for the elements La through Gd, they differ from Rb through K, and Dy through Lu. In particular, the posterior KG1 pyroxenite source exhibits the highest abundances of Rb-K, followed by G2 pyroxenite, followed by MIX1G pyroxenite. The converse is true for the abundances of Dy-Lu, as MIX1G pyroxenite has the highest abundances, followed by G2 pyroxenite and then KG1 pyroxenite. These pyroxenite compositions differ from those used in previous models, a discrepancy that we discuss below.

Posterior distributions of the $^{143}Nd/^{144}Nd$ and $^{206}Pb/^{204}Pb$ compositions of the model sources for each chain are shown in Fig. 10. While all three chains yield nearly identical posterior median Nd isotopic compositions for the model peridotite sources ($^{143}Nd/^{144}Nd$ = 0.513101-0.513105; Fig. 10a; *Supplementary Table 3*), the peridotite posterior median Pb isotopic compositions in these chains exhibit more variability ($^{206}Pb/^{204}Pb$ = 18.421-18.491; Fig. 10b; *Supplementary Table 3*). In contrast, the posterior median Nd and Pb isotopic compositions of the model pyroxenite sources are similar among the three chains ($^{143}Nd/^{144}Nd$ = 0.513007-0.513009; $^{206}Pb/^{204}Pb$ = 18.879-18.881; Fig. 10; *Supplementary Table 3*).

5. Implications for the Reykjanes Peninsula mantle source

5.1. Roles of mantle potential temperature and pyroxenite abundance

The T_P and pyroxenite abundances shown in Fig. 7a-b indicate that the compositions and volumes of basaltic magmatism along Reykjanes Peninsula are best explained by a source with T_P ~ 1455-1480 °C (corresponding to temperature excesses (ΔT_P) of ~125-150 °C above ambient T_P = 1330 °C; Brown and Lesher, 2016) and modest pyroxenite abundances (~6-8%). As the G2, MIX1G, and KG1 pyroxenites used here span most of the range of natural pyroxenite compositions (Fig. 1), this is a robust result that does not depend upon the type of pyroxenite in the source. The modest differences in T_P and Φ_{px} between the different pyroxenite lithologies simply reflect differences in their melting behaviors-G2 pyroxenite is more fertile than either KG1 or MIX1G (G2 melts to completion whereas the others melt to similar, but lower extents; Appendix D). Thus, a G2-bearing source requires less pyroxenite and lower T_P to produce the observed igneous crustal thickness compared to sources containing the other pyroxenites, all else being equal.

Our modelled T_P and Φ_{px} are generally consistent with those used in, or constrained by, previous studies (T_P ~ 1430-1520 °C; ~1-20% pyroxenite; Sobolev et al., 2007; Stracke and Bourdon, 2009; Koornneef et al., 2012a; Rudge et al., 2013; Brown and Lesher, 2014; Shorttle et al., 2014; Lambart, 2017). Of those studies focused on constraining T_P and Φ_{px} simultaneously, Shorttle et al. (2014) and Matthews et al. (2016) predicted the most similar
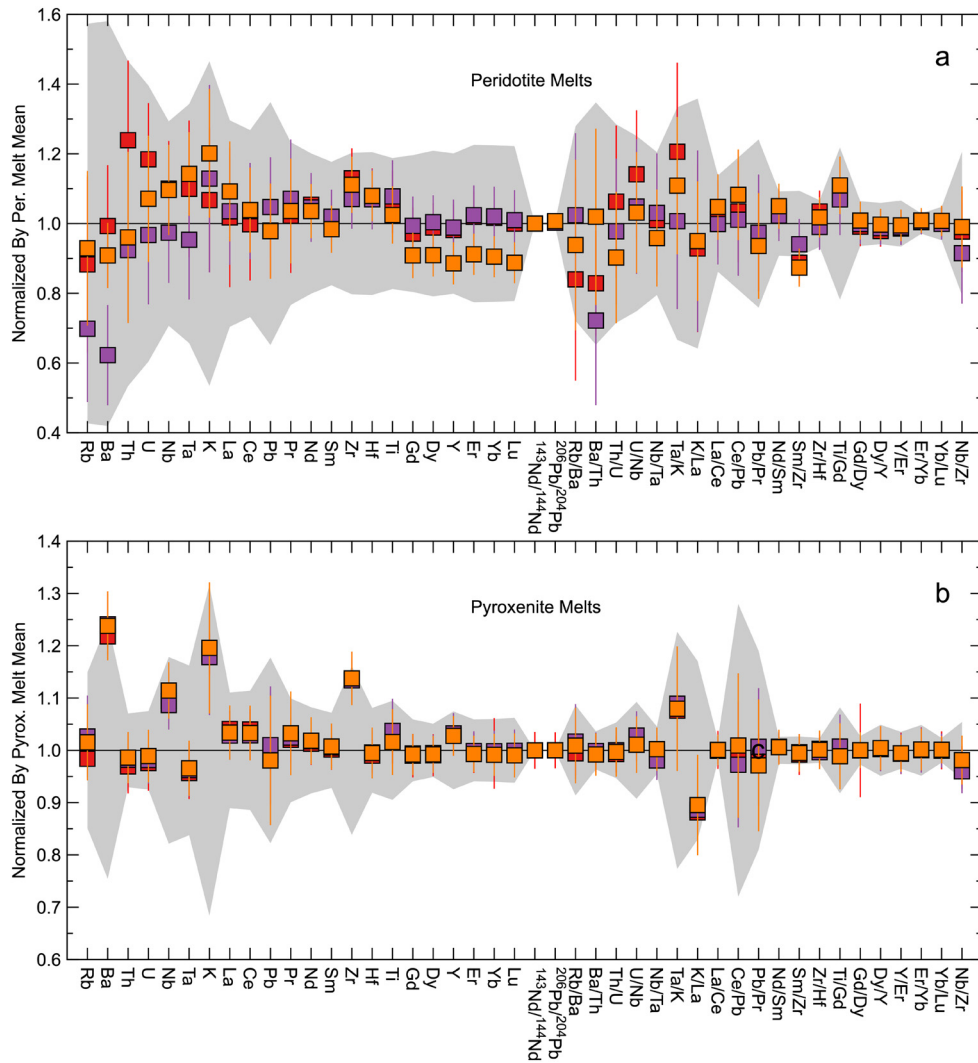
Fig. 6. Model fits to end-member **a)** peridotite melt and **b)** pyroxenite melt compositions. Models and their 1 S.D. are normalized by the mean values from the peridotite- and pyroxenite-derived melts from Reykjanes Peninsula, respectively. The symbols and grey field represent the equivalent information as in Fig. 5.
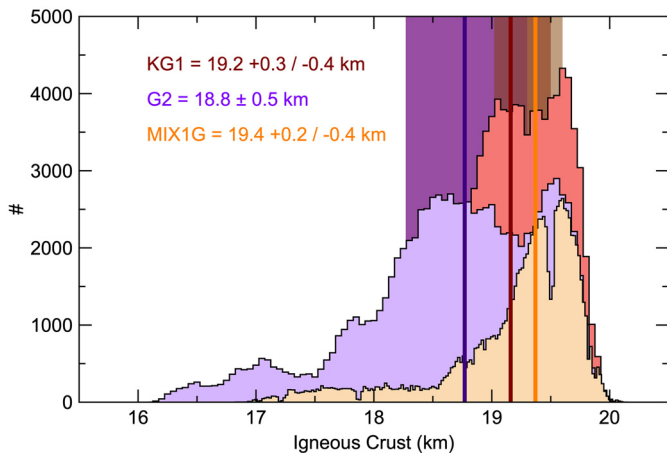

Fig. 7. Posterior histogram of model igneous crustal thickness for the three pyroxenite Markov chains. Median values and the 50% of models falling between the upper and lower quartiles are listed in the figure and are denoted by the vertical lines and colored bands, respectively. Colors are as in Figs. 5 and 6.

T_P and G2 and KG1 pyroxenite abundances to those found in our inversion ($T_P \sim$ 1450-1480 °C; ~8% G2; ~9-12% KG1). However, in developing models to match crustal thickness and estimates

of the proportion of pyroxenite-derived melt comprising the bulk crust from geochemistry (X_{px}), these authors also argued that the source must contain 20-50% harzburgite. As shown in Appendix E, our inversions do not require harzburgite because we modelled melt compositions directly (section 3.2.1) instead of attempting to match a specific estimate of X_{px}. Differences between the two approaches are illustrated in Appendix E.

5.2. Peridotite and pyroxenite source trace element compositions

As shown in Fig. 9, the trace element composition of the model peridotite source is similar for the three chains, and thus does not depend on the type of pyroxenite used in the modeling. This is to be expected because the same peridotite lithology was used in each of the chains. In contrast, the most incompatible (Rb-K) and least incompatible (Dy-Lu) pyroxenite trace element compositions do differ. Given the similar T_P and Φ_{px} for the three chains, these differences relate to differences in the fertility and mineralogies of the pyroxenites. Very incompatible element concentrations are more sensitive to the extent of melting than the less incompatible elements, and thus are sensitive to the fertility of the pyroxenite lithology. Because G2 and KG1 melt to larger extents than MIX1G (Appendix D), their Rb-K concentrations are required to be higher than those of MIX1G to produce melts that match the observed
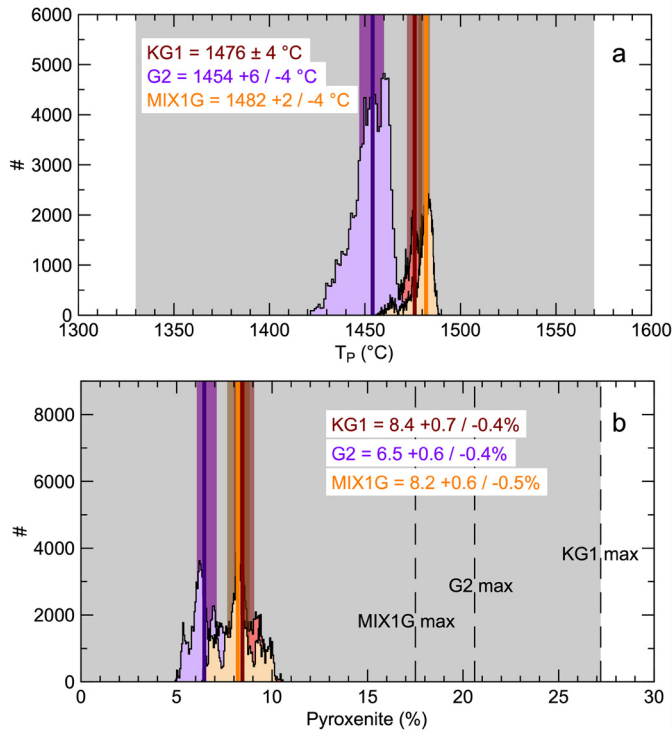
Fig. 8. Posterior distributions of the key model parameters **a**) potential temperature and **b**) pyroxenite abundance. Median values and upper and lower quartiles are given in the figures and shown by vertical lines and colored bands. Colors are as in Figs. 5–7. Grey bands denote range of the parameter's *prior probability distribution*. In b), the upper end of the pyroxenite abundance *prior probability distribution* depends upon the type of pyroxenite (see text). Maximum values for the three pyroxenites are shown as black dashed lines for $T_P = 1570\,°C$.
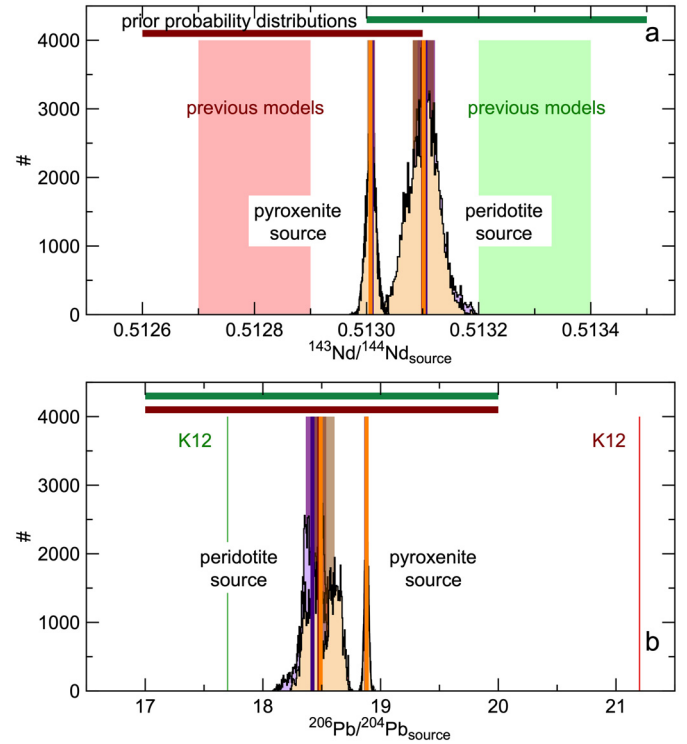

Fig. 10. Posterior distributions of the **a**) $^{143}Nd/^{144}Nd$ and **b**) $^{206}Pb/^{204}Pb$ compositions of the model peridotite and pyroxenite sources. Median values and upper and lower quartiles are given in the figures and shown by vertical lines and colored bands. Colors are as in Figs. 5–8. The green and red fields in panel a denote the range of values for the peridotite and pyroxenite sources, respectively, used in previous forward modeling at Iceland (Koornneef et al., 2012a; Lambart, 2017; Rudge et al., 2013; Stracke and Bourdon, 2009; Brown and Lesher, 2014). The green and red vertical bars in panel b denote the Pb isotopic compositions of the peridotite and pyroxenite sources, respectively, used in previous forward modeling (K12 = Koornneef et al., 2012a). In both panels, the ranges of the *prior probability distributions* for the pyroxenite and peridotite isotopic compositions are given by the horizontal red and green bars, respectively. Note that they are the same for $^{206}Pb/^{204}Pb$.

+ clinopyroxene + garnet ± spinel), are also important, as mineralogy affects melting reactions and bulk mineral-melt partition coefficients governing the distribution of elements between solid source and melt.

The effects of source mineralogy are also responsible for the differences in the least incompatible elements between the pyroxenites. The fractionations of Dy-Lu (Fig. 9) are attributable to differing proportions of garnet in each pyroxenite as Dy-Lu are increasingly compatible in garnet (with Lu more compatible than Dy). Because MIX1G contains the highest proportion of garnet, this pyroxenite source is required to have higher concentrations of Dy-Lu than the other pyroxenites (and higher primitive mantle-normalized Lu/Dy) to produce melts that match the Dy-Lu systematics of the pyroxenite-derived basalts along the Reykjanes Peninsula.

In Fig. 9 we also compare our inverted trace element compositions to those used in previous forward models of Iceland (Koornneef et al., 2012a; Lambart, 2017; Rudge et al., 2013; Stracke and Bourdon, 2009; Brown and Lesher, 2014). In general, these models assumed a depleted MORB mantle for the initial trace element composition of the peridotite source, while the composition of the pyroxenite was based on forward models of recycling of oceanic crust/lithosphere of an assumed mean age (typically 2 Ga). As shown in Fig. 9, our inversion results show that previous assumptions about the trace element composition of the peridotite source were indeed reasonable. However, our modeling further predicts that the pyroxenite source is more than an order of magnitude more enriched in the most incompatible elements (Rb to Ce) than
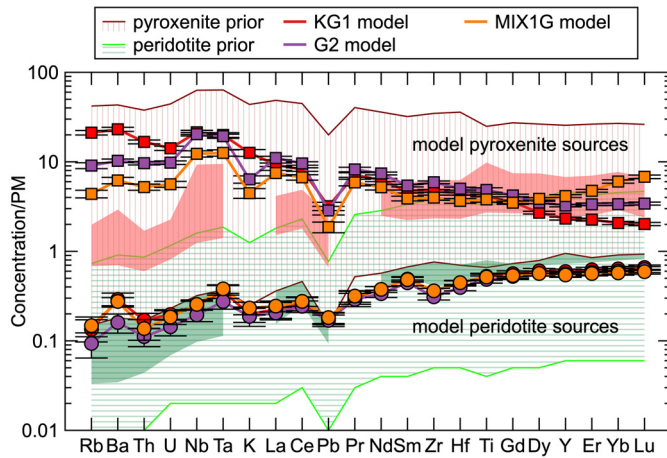

Fig. 9. Mean ±1 S.D. uncertainties on primitive mantle (McDonough and Sun, 1995) normalized posterior peridotite and pyroxenite source trace element compositions. Green and red fields denote the ranges of peridotite and pyroxenite trace element compositions utilized in previous forward modeling at Iceland (Koornneef et al., 2012a; Lambart, 2017; Rudge et al., 2013; Stracke and Bourdon, 2009; Brown and Lesher, 2014). The *prior probability distribution* for the pyroxenite trace elements is given by the red vertical hachure (bounded by red curves). The *prior probability distribution* for the peridotite trace elements is given by the green horizontal hachure (bounded by green curves).

Rb-K concentrations in the pyroxenite-derived basalts. In this context, G2 should have the highest concentrations of the very incompatible elements since it melts to completion, all else being equal. However, KG1 has higher very incompatible element concentrations, indicating that differences in the modal mineralogies of G2 (clinopyroxene + garnet) and KG1 (olivine + orthopyroxene

previously considered. It is important to appreciate that the inversion requires the pyroxenite source to be this enriched (and undergo relatively large extents of melting; Appendix D) to explain the compositions of the end-member pyroxenite-derived melts *and* bulk crust composition for the most probable values of T_P and Φ_{px}. The implications of this enrichment are considered below.

5.3. Peridotite and pyroxenite source isotopic compositions and source implications

In constructing the *likelihood* function we assumed that the end-member peridotite- and pyroxenite-derived basalts erupted along Reykjanes Peninsula have the same isotopic compositions as their respective source lithologies (Shorttle and Maclennan, 2011; Shorttle et al., 2014). Thus, the isotopic compositions of the peridotite and pyroxenite sources shown in Fig. 10 simply reflect those of the primitive basalts used in the likelihood function (see Fig. 5a-b). The distributions and relatively small uncertainties for the peridotite and pyroxenite $^{143}Nd/^{144}Nd$ and pyroxenite $^{206}Pb/^{204}Pb$ compositions reflect the general consistency of these isotopic compositions in the primitive peridotite- and pyroxenite-derived basalts. Conversely, the increased variability in the peridotite $^{206}Pb/^{204}Pb$ distribution (Fig. 10b) is a consequence of the $^{206}Pb/^{204}Pb$ compositions of the primitive peridotite-derived basalts being quite heterogeneous, resulting in a rather large standard deviation for this observational constraint (*Supplementary Table 1*).

As shown in Fig. 10, the modelled ranges for the Nd and Pb isotopic compositions of the peridotite and pyroxenite sources span smaller ranges than the values employed in previous forward models at Iceland (Koornneef et al., 2012a; Lambart, 2017; Rudge et al., 2013; Stracke and Bourdon, 2009; Brown and Lesher, 2014). This is because these previous models assumed that all Iceland basalt compositions are mixtures of peridotite- and pyroxenite-derived melts; that is, no "pure" pyroxenite (and peridotite) melts are represented in Iceland basalt compositions. However, as noted above, melt inclusion studies show that a bimodal distribution of depleted and enriched melts is supplied to the crust, indicating a lack of mixing between peridotite- and pyroxenite-derived melts (Maclennan, 2008a, 2008b). Thus, if the end-member melt compositions do reflect a lack of detectable mixing between the peridotite and pyroxenite-derived melts, then the isotopic compositions used in the previous models are incorrect.

Despite these differences, our modelled peridotite Nd and Pb isotope compositions do overlap with the mean ± 1 S.D. of normal MORB (Gale et al., 2013). This similarity, along with the DMM-like trace element compositions noted above, suggests the peridotite source is similar to the average upper mantle feeding the global spreading ridges. Compared to previous studies, the higher Nd and lower Pb isotopic compositions of the pyroxenite source found here suggest a relatively younger mean age if the source is recycled oceanic crust. However, the pyroxenite source is not likely to be recycled oceanic crust given that the incompatible element compositions of the model pyroxenites are more enriched than the most extreme enriched-MORB (Gale et al., 2013) and that primitive pyroxenite-derived melts at Iceland have MgO contents too high to be derived by partial melting of eclogitized basaltic oceanic crust (Shorttle and Maclennan, 2011). Instead, we hypothesize the pyroxenite's very incompatible element enrichment and high MgO content originates from metasomatism of a depleted peridotite source by low degree partial melts induced by volatiles at deeper levels of the melting regime (e.g., Dasgupta et al., 2007). Given the pyroxenite's overall incompatible trace element enrichment and somewhat depleted isotopic compositions, this event must have occurred relatively recently. Speculation aside, it is clear

that *a priori* assumptions of pyroxenite source composition based on forward petrogenetic and recycling models can be misleading.

6. Implications for forward modeling

In addition to constraining mantle conditions beneath the Reykjanes Peninsula, the modeling results presented above also have important implications for the future application of forward and inverse models at Iceland and elsewhere. Firstly, the similarities in estimated T_P and Φ_{px} between our inverse modeling and previous forward models that explicitly considered source buoyancy and used crustal thickness as a modeling constraint (Brown and Lesher, 2014; Shorttle et al., 2014; Matthews et al., 2016) indicate that igneous crustal thickness and source buoyancy are fundamentally important factors that should be considered in future forward and inverse modeling applications. A corollary of this is that reliable constraints on T_P and Φ_{px} can be made using forward models (such as REEBOX PRO) if crustal thickness and source buoyancy are explicitly used in the modeling (although uncertainties in these parameters may remain difficult to constrain).

Secondly, although a KG1-like pyroxenite has been inferred as the pyroxenite source beneath Iceland (Shorttle and Maclennan, 2011; Lambart, 2017; Neave et al., 2018), an important outcome of our modeling is that the three pyroxenites used in the modeling yielded model melt compositions that fit the observations equally well within the observational uncertainties. Thus, from the trace element and isotope perspective, each pyroxenite is as likely as the other (without any independent *a priori* constraints on their compositions). This outcome contrasts with recent forward modeling at Iceland (Lambart, 2017), which also considered three different pyroxenites. Assuming an isochemical source consisting of 10% recycled MORB and 90% DMM, Lambart argued for a KG1-like pyroxenite because it yielded better model fits to the chemical/isotopic data than sources containing the other two pyroxenite (G2 and KG2 pyroxenite). However, broader ranges of T_P, Φ_{px}, or initial trace element and isotopic compositions for the peridotite and pyroxenite sources were not explored, which combined with our results, draws into question the reliability of constraining the type of pyroxenite present in the mantle source based on a fixed or limited range of assumed parameters. At present, correlations between major element, trace element, and isotopic compositions of primitive basalts continue to provide the best constraints on plausible pyroxenite compositions and their melting behaviors (e.g., Shorttle and Maclennan, 2011), and can be used to guide the type of pyroxenite employed in future forward and inverse modeling.

7. Conclusions

Here we have developed a new inverse mantle melting model that constrains mantle potential temperature, lithologic abundance (e.g. peridotite and pyroxenite), and the initial trace element and isotopic compositions of the source lithologies by coupling a Metropolis Markov chain Monte Carlo sampling method with the forward melting model REEBOX PRO. This approach constrains the distributions of model input parameters producing models that fit a number of geochemical and geophysical observations within their uncertainties. To demonstrate the model's capabilities, we have applied it to constrain the mantle source conditions beneath the Reykjanes Peninsula in southwest Iceland. Considering a source containing peridotite and one of three different pyroxenites spanning much of the range of natural pyroxenites (G2, MIX1G, or KG1 pyroxenite), we found that magmatism there is best explained by elevated T_P (~125-150 °C above ambient mantle), and ~6-8% pyroxenite. The trace element composition of the inverted peridotite source is similar to depleted MORB mantle compositions employed in previous forward modeling studies of Iceland, but the inverted

pyroxenite source has very incompatible trace element concentrations that are higher than previously considered for Iceland. These results indicate that previous assumptions about the petrogenetic history of the pyroxenite source beneath Iceland require further consideration, as does the application of forward and inverse models in the future. Given the range of lithologies included in REEBOX PRO, and the flexibility of the MCMC method, this inverse modeling approach has broad applicability to not only hot, pyroxenite-bearing mantle domains, but elsewhere where hydrous or carbonated peridotite sources may be important.

Acknowledgements

Declaration of competing interest

The authors declare that they have no known competing financial interests or personal relationships that could have appeared to influence the work reported in this paper.

Appendix A. KG1 melting parameterization

To incorporate KG1 pyroxenite (Kogiso et al., 1998) in REEBOX PRO, we utilized the MELT-Px program (Lambart et al., 2016) to quantify its melting behavior. Because modeling melt compositions requires knowledge of the source mineralogy and melting reaction coefficients (both of which are not provided by MELT-Px), we applied the methods described in *Appendix B* of Brown and Lesher (2016) to constrain mineral modes as functions of pressure and melt depletion (which consequently allows calculation of melting reaction coefficients). This requires information about the mineral modes along the KG1 solidus and the extents of melting required to exhaust each phase at any given pressure. We quantified these values using ThermoCalc (Powell et al., 1998) and the Jennings and Holland (2015) thermodynamic database using the KG1(8) bulk composition modelled by Jennings et al. (2016). To ensure consistency with the MELT-Px melting parameterization (which depends on the melt fraction at which clinopyroxene is exhausted from the residue, $F_{cpx-out}$), we renormalized the phase-out boundaries predicted by ThermoCalc to be consistent with $F_{cpx-out}$ predicted by the MELTS-Px model. For the phase out boundaries, we find

$$F^{KG1}_{ol-out} = 100 \quad P < 2.3 \text{ GPa} \tag{A.1}$$

$$F^{KG1}_{ol-out} = -20.27P + 146.62 \quad P \geq 2.3 \text{ GPa} \tag{A.2}$$

$$F^{KG1}_{opx-out} = 15.38P + 64.62 \quad P < 2.3 \text{ GPa} \tag{A.3}$$

$$F^{KG1}_{opx-out} = 100 \quad 2.3 \leq P < 3.605 \text{ GPa} \tag{A.4}$$

$$F^{KG1}_{opx-out} = -30.391P + 209.55 \quad P \geq 3.605 \text{ GPa} \tag{A.5}$$

$$F^{KG1}_{opx-in} = 0 \quad P \leq 2.364 \text{ GPa} \tag{A.6}$$

$$F^{KG1}_{opx-in} = 17.21P - 40.684 \quad P > 2.364 \text{ GPa} \tag{A.7}$$

$$F^{KG1}_{cpx-out} = -3.91P^2 + 20.81P + 48.47 \quad P \leq 5 \text{ GPa} \tag{A.8}$$

$$F^{KG1}_{gt-out} = 0 \quad P < 2.186 \text{ GPa} \tag{A.9}$$

$$F^{KG1}_{gt-out} = 360.24P - 787.43 \quad 2.816 \leq P < 2.3 \text{ GPa} \tag{A.10}$$

$$F^{KG1}_{gt-out} = 49.38P - 78.03 \quad 2.3 \leq P < 3.605 \text{ GPa} \tag{A.11}$$

$$F^{KG1}_{gt-out} = 100 \quad P \geq 3.605 \text{ GPa} \tag{A.12}$$

$$F^{KG1}_{sp-out} = 1.74P + 30.68 \quad 1 \leq P < 2.282 \text{ GPa} \tag{A.13}$$

$$F^{KG1}_{sp-out} = -231.21P + 562.94 \quad 2.282 \leq P < 2.369 \text{ GPa} \tag{A.14}$$

$$F^{KG1}_{sp-out} = -86.97P + 215.37 \quad 2.369 \leq P < 2.479 \text{ GPa} \tag{A.15}$$

$$F^{KG1}_{sp-out} = 0 \quad P \geq 2.479 \text{ GPa} \tag{A.16}$$

The parameterized solidus mineral modes from ThermoCalc are

$$ol^{KG1}_{solidus} = -0.1398P^2 + 0.8367P + 9.2359 \quad P < 2.185 \text{ GPa} \tag{A.17}$$

$$ol^{KG1}_{solidus} = -46.23P^2 + 237.18P - 287.16 \quad 2.185 \leq P < 2.36 \text{ GPa} \tag{A.18}$$

$$ol^{KG1}_{solidus} = -5.9053 + 35.244P - 35.137 \quad 2.36 \leq P < 2.49 \text{ GPa} \tag{A.19}$$

$$ol^{KG1}_{solidus} = 0.0254P + 15.955 \quad P \geq 2.49 \text{ GPa} \tag{A.20}$$

$$opx^{KG1}_{solidus} = -1.1215P^2 - 7.2795P + 38.14 \quad P < 2.185 \text{ GPa} \tag{A.21}$$

$$opx^{KG1}_{solidus} = 173.66P^2 + 885.15P + 1122 \quad 2.185 \leq P < 2.36 \text{ GPa} \tag{A.22}$$

$$opx^{KG1}_{solidus} = 0 \quad P \geq 2.36 \text{ GPa} \tag{A.23}$$

$$cpx^{KG1}_{solidus} = 1.121P^2 + 7.198P + 45.907 \quad P < 2.185 \text{ GPa} \tag{A.24}$$

$$cpx^{KG1}_{solidus} = 17.753P^2 - 107.92P + 217.95 \quad 2.185 \leq P < 2.49 \text{ GPa} \tag{A.25}$$

$$cpx^{KG1}_{solidus} = 0.3327P^2 - 4.691P + 68.857 \quad P \geq 2.49 \text{ GPa} \tag{A.26}$$

$$sp^{KG1}_{solidus} = 0.1404P^2 - 0.7546P + 6.7161 \quad P < 2.185 \text{ GPa} \tag{A.27}$$

$$sp^{KG1}_{solidus} = 46.573P^2 - 239.33P + 306.35 \quad 2.185 \leq P < 2.36 \text{ GPa} \tag{A.28}$$

$$sp^{KG1}_{solidus} = 5.7843P^2 - 34.792P + 50.77 \quad 2.36 \leq P < 2.49 \text{ GPa} \tag{A.29}$$

$$sp^{KG1}_{solidus} = 0 \quad P \geq 2.49 \text{ GPa} \tag{A.30}$$

$$gt^{KG1}_{solidus} = 0 \quad P < 2.185 \text{ GPa} \tag{A.31}$$

$$gt^{KG1}_{solidus} = -208.15P^2 + 1069.9P - 1344.2 \quad 2.185 \leq P < 2.36 \text{ GPa} \tag{A.32}$$

$$gt^{KG1}_{solidus} = -19.959P^2 + 119.72P - 149.59 \quad 2.36 \leq P < 2.49 \text{ GPa} \tag{A.33}$$

$$gt^{KG1}_{solidus} = -0.32931 + 4.6407P + 15.234 \quad P \geq 2.49 \text{ GPa} \tag{A.34}$$

From these equations, we quantified the mineral modes as functions of P and F using the approach outlined by equations *B29-B31* in Brown and Lesher (2016). Finally, the density of the KG1 lithology was quantified using the Stixrude and Lithgow-Bertelloni (2011) thermodynamic database with PerpleX (Connolly, 1990, 2005).

Appendix B. Fractionation correction for peridotite- and pyroxenite-derived melts

To constrain the effects of olivine crystallization on primitive low- and high-Nb/Zr lavas (representing the peridotite- and pyroxenite-derived melts, respectively), we utilized the method of McKenzie and O'Nions (1991), which requires an estimate of the MgO and FeO content of an undifferentiated primary magma. Using only samples for which data for all major elements were provided, we identified plausible primary magma compositions for both the low and high Nb/Zr groups using PRIMELT2 (Herzberg and Asimow, 2008). Because PRIMELT2 requires ferrous iron (FeO) as an input, and because most of the samples in our dataset report total iron (FeO_T) instead of FeO, we recast FeO_T into FeO and Fe_2O_3 using the method described by Herzberg and Asimow (2008) assuming $Fe_2O_3/TiO_2 = 0.5$. For the low Nb/Zr group, PRIMELT2 identified picrite sample ICE 4B (see *Supplementary Information*) as a potential primary magma assuming it was derived from a peridotite source having MgO = 38.12 wt.% and FeO = 8.02 wt.% (i.e., KR4003; Walter (1998)). For the high Nb/Zr group, the sample with the highest MgO (sample ICE3; see *Supplementary Information*) was identified as a potential primary magma assuming it was derived from an enriched peridotite source with MgO = 23.6 wt.% and FeO = 9.77 wt.% like KG1 pyroxenite (Kogiso et al., 1998). Assuming each trace element is perfectly incompatible in olivine, we calculated a primary melt composition by multiplying each measured (i.e., original) concentration by $(1 - X)$ (Maclennan et al., 2001), where X is the calculated extent of crystallization (McKenzie and O'Nions, 1991).

Appendix C. Identifying conservative trace element ratios for bulk crust composition

Iceland lavas have experienced different degrees of crystallization prior to eruption. Thus, to constrain the mean bulk igneous crust composition for Reykjanes Peninsula using evolved, low MgO basalts (5-7 wt.%) from the GEOROC dataset, we employ conservative trace element ratios unaffected by fractional crystallization. Shorttle et al. (2014) also identified conservative incompatible trace element ratios in their work at Iceland, but utilized a smaller (and different) set of incompatible elements than is incorporated in REEBOX PRO. To utilize as many elements as possible from REEBOX PRO to model the bulk crust composition, we constructed a 24×24 matrix of trace element ratios utilizing all 24 elements included in REEBOX PRO. Using the same mineral-melt coefficients and crystallization model employed by Shorttle et al. (2014), we then forward modelled the magnitude of fractionation of each trace element ratio after 80% crystallization (corresponding to basalts having ~5 wt.% MgO; Maclennan et al., 2001), assuming an initial value of unity for the uncrystallized primary magma (i.e., 100% melt fraction remaining). Thus, the ratio of any two elements provides an estimate of the magnitude the ratio has been fractionated due to crystallization of wehrlite (from 14 to 9.5 wt.% MgO) followed by gabbro (from 9.5 to 5 wt.% MgO) (Maclennan et al., 2001). The corresponding magnitudes of fractionation for each ratio are shown in Fig. C1.

We filtered the resulting ratios by initially selecting only those ratios that exhibited <20% relative fractionation between 0 and 80% crystallization. Notably, all ratios involving Sr and Eu were excluded, as these are readily incorporated into plagioclase (i.e., during gabbro fractionation for lavas with less than ~9.5 wt.% MgO; Maclennan et al. (2001)) and were thus significantly fractionated. This step yielded 462 potentially viable ratios (Fig. C1). Given the role of concurrent mixing and crystallization in generating the evolved lavas that provide a proxy for the bulk crust composition, any ratio of similarly incompatible trace elements
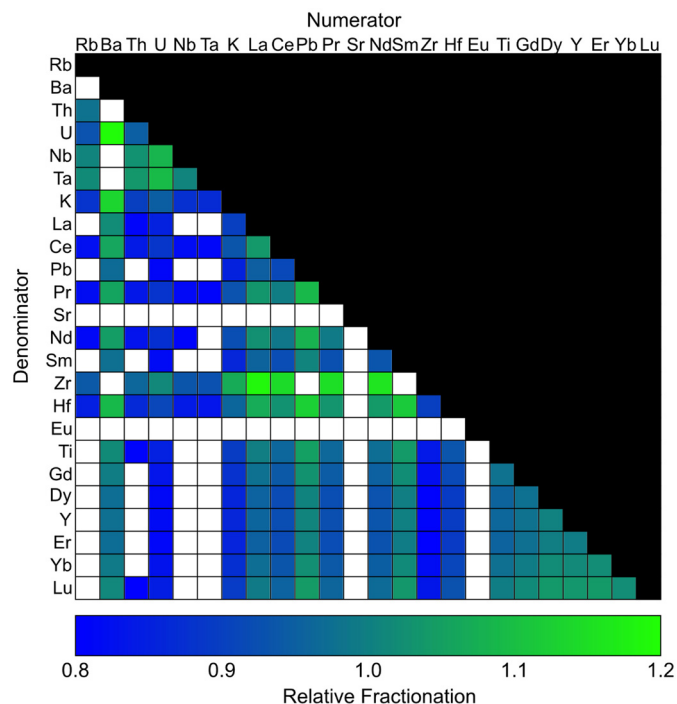

Fig. C1. Identification of candidate incompatible trace element ratios for use in quantifying mean bulk crust composition. Color-coded boxes denote element pairs exhibiting <20% relative enrichment or depletion due to 80% fractional crystallization of wehrlite (from 14 to 9.5 wt.% MgO) followed by gabbro (from 9.5 to 5 wt.% MgO) (Maclennan et al., 2001). White boxes denote element-element ratios with relative enrichments/depletions ≥20%. Of the 462 ratios identified here, we utilize 72 in the likelihood function.

(and radiogenic isotopic compositions) in the bulk crust should lie intermediate to the compositions of the peridotite and pyroxenite melts that are being mixed to form the bulk crust. Thus, if any ratio is fractionated during crystallization, or is affected by secondary alteration, it may result in the bulk crust composition lying outside of the bounds defined by the peridotite and pyroxenite melts. We thus identified and excluded all ratios that violated this constraint (outside their uncertainties) within the 462 potentially viable candidates. To further narrow the number of ratios and to ensure numerical stability, we filtered the remaining ratios further to include only those that exhibit <20% relative standard deviations, while making sure that each element (except Sr and Eu) was utilized in more than one bulk crust ratio (with the exception of Pb, which is used in only one bulk crust ratio because of the filtering applied). Thus, out of a possible 462 element-element ratios that we considered for constraining the bulk crust composition, only 72 were included in the likelihood function (summarized in *Supplementary Table 1*).

Appendix D. Melting column lengths

Fig. D1 shows the posterior histograms of the fractions of the melting column over which instantaneous peridotite and pyroxenite melts are accumulated to produce the end-member peridotite- and pyroxenite-derived melts (assuming instantaneous melt accumulation begins at the base of the column, and the top of the column equals unity). Here, the modeling results indicate that peridotite instantaneous melts are accumulated over the vast majority (>90%) of the peridotite melting column, independent of the type of pyroxenite used in the modeling. Assuming the median T_P and peridotite abundances for the three different pyroxenite Markov chains, this corresponds to ~19-25% total melting of the peridotite source in these chains. In contrast, the manner of pyroxenite melt
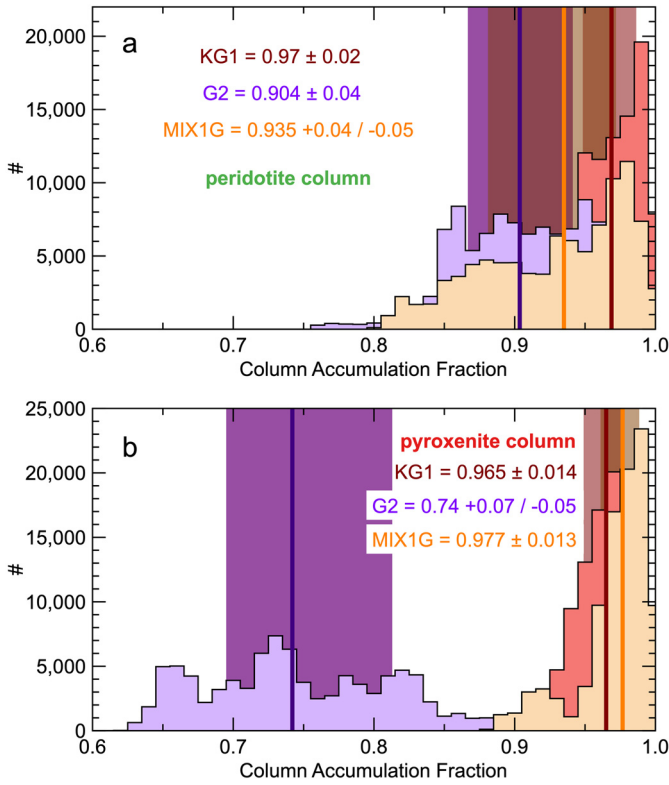
Fig. D1. Posterior distributions of the fractions of the melting column over which instantaneous **a**) peridotite and **b**) pyroxenite melts are accumulated to produce the end-member peridotite- and pyroxenite-derived melts (assuming instantaneous melt accumulation begins at the base of the column). A melting column is defined as the pressure interval between the solidus and the base of the igneous crust (see Fig. 3). A fraction of unity means that instantaneous melts were accumulated over the length of the entire melting column. Median and upper and lower quartile values are shown as vertical lines and colored bands, respectively, as well as listed within the figure. All colors as in Figs. 4–8 in the main text.

accumulation appears to be more variable. For example, instantaneous KG1 and MIX1G pyroxenite melts are both accumulated over almost the entirety of their melting columns (corresponding to total extents of melting of ∼81-84.2% and ∼68.1-72.5%, respectively), whereas instantaneous G2 pyroxenite melts are accumulated over a much broader range, and extracted deeper in the melting column (∼75% of the way toward the top of the melting column). Given that G2 pyroxenite is more productive than either KG1 or MIX1G, the total extent of G2 pyroxenite melting is 100% by reaching this portion of the melting column (assuming the median T_P and peridotite abundances for the different Markov chains). Thus, G2 pyroxenite is melted entirely out of the source around this melting column depth. All points within the melting column above the disappearance of G2 melting are therefore equivalent in terms of the composition of the aggregated instantaneous G2 pyroxenite melts. This is because no instantaneous G2 melts are produced or accumulated above the depth at which G2 is melted out of the source. Thus, the posterior distribution of G2 melt accumulation does not provide any useful insight into the process of G2 pyroxenite melt accumulation.

The generation of depleted Reykjanes Peninsula lavas by large extents of peridotite melting (i.e., ∼20%) is consistent with previous work (Gurenko and Chaussidon, 1995; Neave et al., 2018), but large extents of melting for the enriched (pyroxenite) melts is not. Instead, these earlier studies suggested that the enriched lavas formed by low degree melting of the source. This discrepancy arises because these previous studies assumed the enriched melts were generated from a peridotite source with an initial trace element composition of either depleted mantle, or primitive man-

tle, both of which would require low melting extents to produce the incompatible element enrichments observed in the enriched melts.

Appendix E. The role of harzburgite

Some workers (Shorttle et al., 2014; Matthews et al., 2016) have argued that harzburgite could constitute a potentially significant proportion of the Iceland mantle source (in addition to peridotite and pyroxenite). Shorttle et al. (2014) developed a forward model for sources containing variable proportions of peridotite, pyroxenite, and non-melting harzburgite. These authors showed that for an assumed T_P, the proportions of these lithologies are uniquely constrained by the intersection of contours for the modelled bulk igneous crustal thickness and modelled proportion of pyroxenite-derived melt in the bulk igneous crust (X_{px}) (Fig. 5 in Shorttle et al., 2014). As with our study, these authors used geophysical observations to constrain crustal thickness, and constrained X_{px} by mass balancing the incompatible trace element ratios (such as Nb/Zr) found in the end-member peridotite- and pyroxenite-derived melts with those ratios found in the most evolved lavas (i.e., bulk crust-like)

$$X_{px} = \frac{[(\frac{Nb}{Zr})_{per} - (\frac{Nb}{Zr})_{BC}]}{(\frac{Zr_{px}}{Zr_{per}})[(\frac{Nb}{Zr})_{BC} - (\frac{Nb}{Zr})_{px}] + [(\frac{Nb}{Zr})_{per} - (\frac{Nb}{Zr})_{BC}]}, \quad (E.1)$$

where the subscripts *per*, *px*, and *BC* refer to the end-member peridotite-derived melts, end-member pyroxenite-derived melts, and bulk crust-like melts, respectively. Assuming a crustal thickness of 20 km and $X_{px} = 0.3 \pm 0.1$, Shorttle et al. (2014) and Matthews et al. (2016) showed that the only models matching these constraints contain ∼20-50% harzburgite for T_P ∼ 1450-1480 °C when considering both G2 (∼8% of the source) and KG1 (∼9-12% of the source) pyroxenite.

Although our modelled T_P and use of G2 and KG1 pyroxenite abundances are consistent with these T_P and pyroxenite abundances, our models were able to reconcile the geophysical and geochemical observations for the Reykjanes Peninsula with slightly lower pyroxenite abundances (∼6-8%) and without requiring harzburgite to be present in the source. Although we considered a slightly thinner crustal thickness (18 ± 1.5 km), the primary reason for this discrepancy is that unlike Shorttle et al. (2014) and Matthews et al. (2016), we did not attempt to match a specific estimate of X_{px}. Instead, we matched the melt compositions directly (section 3.2.1).

Like Shorttle et al. (2014) and Matthews et al. (2016), we assumed passive corner flow when quantifying the bulk crustal thickness and composition. Thus, from the melt modeling perspective, X_{px} is quantified by pooling all instantaneous peridotite and pyroxenite melts generated within the triangular melting zone

$$X_{px} = \frac{\Phi_{px} \int_{P_{0_{pyx}}}^{P_c} F_{px} dP}{\Phi_{px} \int_{P_{0_{pyx}}}^{P_c} F_{px} dP + \Phi_{per} \int_{P_{0_{per}}}^{P_c} F_{per} dP}, \quad (E.2)$$

where Φ_{px} and Φ_{per} are the initial mass fractions of pyroxenite and peridotite, respectively, F_{px} and F_{per} are the mass fractions of pyroxenite and peridotite melt, respectively, P_c is the pressure at the base of the crust, $P_{0_{pyx}}$ and $P_{0_{per}}$ are the pyroxenite and peridotite solidus pressures, respectively, and dP is the decompression step size, with the pressure at the base of the crust (P_c) given by the denominator. In this context, we find that our G2, MIX1G, and KG1 models yield $X_{px} = 0.34$, 0.17, and 0.22, respectively when using the median T_P and pyroxenite abundances presented in the
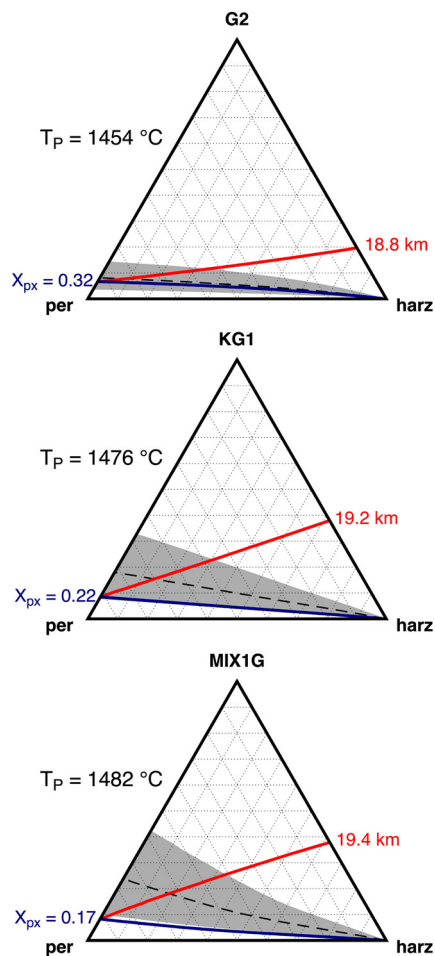
Fig. E1. Ternary diagrams showing forward model results for different combinations of peridotite, pyroxenite (G2, KG1, and MIX1G) and (non-melting) harzburgite in the model mantle source (after Shorttle et al., 2014). Assuming the median T_P values from each Markov chain discussed in the text, the median crustal thicknesses from each respective Markov chain are shown as red contours, and their corresponding X_{px} (quantified using eq. (E.2)) are represented by dark blue contours. The black dashed curves and grey fields represent X_{px} estimates for the Western Volcanic Zone by Shorttle et al. (2014) ($X_{px} = 0.4 \pm 0.2$) quantified using eq. (E.1). See text for discussion.

main text (Fig. E1). Thus, the three different pyroxenites yield different X_{px} despite matching the same geochemical and geophysical observational constraints.

Comparison of eqs. (E.1) and (E.2) shows that they are not equivalent. Whereas eq. (E.2) represents the aggregate composition derived by pooling all *instantaneous* melts from the melting zone, eq. (E.1) represents the aggregate composition derived by mixing the end-member *column-accumulated* peridotite- and pyroxenite-derived melts. Thus, the model outputs (calculated using eq. (E.2)) are not being compared with the correct geochemical information when eq. (E.1) is applied (as done by Shorttle et al. (2014) and Matthews et al. (2016)). The result of this incorrect comparison can be appreciated in Fig. E1, where we plot ternary diagrams for different combinations of source peridotite, pyroxenite, and (non-melting) harzburgite abundance. Each of these plots was constructed by running forward models in REEBOX PRO with different combinations of these lithologies, assuming the median T_P values from each of the three pyroxenite chains discussed in the main text. For each of the three pyroxenites, the median crustal thicknesses from each respective Markov chain are plotted as red contours, with the corresponding X_{px} for each of these crustal thicknesses (calculated using eq. (E.2)) shown by the dark blue contours. Also shown are X_{px} estimates for the Western Volcanic

Zone by Shorttle et al. (2014) ($X_{px} = 0.4 \pm 0.2$; black dashed curve and grey field) calculated using eq. (E.1). In all cases, our crustal thickness and X_{px} curves intersect along the peridotite-pyroxenite join (as expected since we did not include harzburgite). However, if we attempted to match our modelled crustal thicknesses to the X_{px} predicted by Shorttle et al. (2014) instead of matching the melt compositions directly, we would require $\sim$5%, 15%, and $\sim$20% for the G2, KG1, and MIX1G models, respectively (i.e., where the crustal thickness contours intersect the $X_{px} = 0.4$ curves). These results illustrate that care must be taken when relating model outputs to specific geochemical observations.

Appendix F. Supplementary material

Supplementary material related to this article can be found online at https://doi.org/10.1016/j.epsl.2019.116007.

References

Allegre, C.J., Minster, J.F., 1978. Quantitative models of trace element behavior in magmatic processes. Earth Planet. Sci. Lett. 38 (1), 1–25.

Brown, E.L., Lesher, C.E., 2014. North Atlantic magmatism controlled by temperature, mantle composition and buoyancy. Nat. Geosci. 7 (11), 820–824.

Brown, E.L., Lesher, C.E., 2016. REEBOX PRO: a forward model simulating melting of thermally and lithologically variable upwelling mantle. Geochem. Geophys. Geosyst. 17, 3929–3968.

Cawthorn, R.G., 1975. Degrees of melting in mantle diapirs and the origin of ultrabasic liquids. Earth Planet. Sci. Lett. 27 (1), 113–120.

Connolly, J.A.D., 1990. Multivariable phase diagrams: an algorithm based on generalized thermodynamics. Am. J. Sci. 290, 666–718.

Connolly, J.A.D., 2005. Computation of phase equilibria by linear programming: a tool for geodynamic modeling and its application to subduction zone decarbonation. Earth Planet. Sci. Lett. 236 (1–2), 524–541.

Darbyshire, F.A., White, R.S., Priestley, K.F., 2000. Structure of the crust and uppermost mantle of Iceland from a combined seismic and gravity study. Earth Planet. Sci. Lett. 181 (3), 409–428.

Dasgupta, R., Hirschmann, M.M., Smith, N.D., 2007. Water follows carbon: CO_2 incites deep silicate melting and dehydration beneath mid-ocean ridges. Geology 35 (2), 135–138.

Gale, A., Dalton, C.A., Langmuir, C.H., Su, Y., Schilling, J.-G., 2013. The mean composition of ocean ridge basalts. Geochem. Geophys. Geosyst. 14 (3), 489–518.

Gallagher, K., Charvin, K., Nielsen, S.B., Sambridge, M., Stephenson, J., 2009. Markov chain Monte Carlo (MCMC) sampling methods to determine optimal models, model resolution and model choice for Earth Science problems. Mar. Pet. Geol. 26, 525–535.

Gast, P.W., Tilton, G.R., Hedge, C., 1964. Isotopic composition of lead and strontium from Ascension and Gough Islands. Science 145, 1181–1185.

Gee, M.A.M., Thirlwall, M.F., Taylor, R.N., Lowry, D., Murton, B.J., 1998. Crustal processes: major controls on Reykjanes Peninsula lava chemistry, SW Iceland. J. Petrol. 39 (5), 819–839.

Gilks, W.R., Richardson, S.H., Spiegelhalter, D. (Eds.), 1996. Markov Chain Monte Carlo in Practice. Chapman and Hall/CRC, London.

Gurenko, A.A., Chaussidon, M., 1995. Enriched and depleted primitive melts included in olivine from Icelandic tholeiites: origin by continuous melting of a single mantle column. Geochim. Cosmochim. Acta 59 (14), 2905–2917.

Herzberg, C.T., Asimow, P.D., 2008. Petrology of some oceanic island basalts: PRIMELT2.XLS software for primary magma calculation. Geochem. Geophys. Geosyst. 9 (9).

Hofmann, A.W., Feigenson, M., 1983. Case studies on the origin of basalt. I. Theory and reassessment of Grenada basalts. Contrib. Mineral. Petrol. 84, 382–389.

Jennings, E.S., Holland, T.J.B., 2015. A simple thermodynamic model for melting of peridotite in the system NCFMASOCr. J. Petrol. 56 (5), 869–892.

Jennings, E.S., Holland, T.J.B., Shorttle, O., Maclennan, J., Gibson, S.A., 2016. The composition of melts from a heterogeneous mantle and the origin of ferropicrite: application of a thermodynamic model. J. Petrol. 57, 2289–2310.

Klein, E.M., Langmuir, C.H., 1987. Global correlations of ocean ridge basalt chemistry with axial depth and crustal thickness. J. Geophys. Res. 92 (B8), 8089–8115.

Kogiso, T., Hirose, K., Takahashi, E., 1998. Melting experiments on homogeneous mixtures of peridotite and basalt: application to the genesis of ocean island basalts. Earth Planet. Sci. Lett. 162 (1), 45–61.

Koornneef, J.M., Stracke, A., Bourdon, B., Meier, M.A., Jochum, K.P., Stoll, B., Grönvold, K., 2012a. Melting of a two-component source beneath Iceland. J. Petrol. 53 (1), 127–157.

Koornneef, J.M., Stracke, A., Bourdon, B., Grönvold, K., 2012b. The influence of source heterogeneity on the U-Th-Pa-Ra disequilibria in post-glacial tholeiites from Iceland. Geochim. Cosmochim. Acta 87 (C), 243–266.

Lambart, S., 2017. No direct contribution of recycled crust in Icelandic basalts. Geochem. Perspect. Lett. 4, 7–12.

Lambart, S., Laporte, D., Schiano, P., 2009. An experimental study of pyroxenite partial melts at 1 and 1.5 GPa: implications for the major-element composition of Mid-Ocean Ridge Basalts. Earth Planet. Sci. Lett. 288 (1–2), 335–347.

Lambart, S., Baker, M.B., Stolper, E.M., 2016. The role of pyroxenite in basalt genesis: melt-PX, a melting parameterization for mantle pyroxenites between 0.9 and 5 GPa. J. Geophys. Res. 121.

Liu, B., Liang, Y., 2017. An introduction of Markov chain Monte Carlo method to geochemical inverse problems: reading melting parameters from REE abundances in abyssal peridotites. Geochim. Cosmochim. Acta 203, 216–234.

Maclennan, J., McKenzie, D.P., Grönvold, K., Slater, L., 2001. Crustal accretion under northern Iceland. Earth Planet. Sci. Lett. 191 (3), 295–310.

Maclennan, J., 2008a. Lead isotope variability in olivine-hosted melt inclusions from Iceland. Geochim. Cosmochim. Acta 72 (16), 4159–4176.

Maclennan, J., 2008b. Concurrent mixing and cooling of melts under Iceland. J. Petrol. 49 (11), 1931–1953.

Matthews, S., Shorttle, O., Maclennan, J., 2016. The temperature of the Icelandic mantle from olivine-spinel aluminum exchange thermometry. Geochem. Geophys. Geosyst. 17.

McDonough, W.F., Sun, S.S., 1995. The composition of the Earth. Chem. Geol. 120, 223–253.

McKenzie, D.P., O'Nions, R.K., 1991. Partial melt distributions from inversion of rare earth element concentrations. J. Petrol. 32 (5), 1021–1091.

Metropolis, N., Rosenbluth, A.W., Rosenbluth, M.N., Teller, A.H., Teller, E., 1953. Equation of state calculations by fast computing machines. J. Chem. Phys. 21, 1087–1092.

Minster, J.F., Allegre, C.J., 1978. Systematic use of trace elements in igneous processes. Part III. Inverse problem of batch partial melting in volcanic suites. Contrib. Mineral. Petrol. 68, 37–52.

Neave, D.A., Shorttle, O., Oeser, M., Weyer, S., Kobayashi, K., 2018. Mantle-derived trace element variability in olivines and their melt inclusions. Earth Planet. Sci. Lett. 483, 90–104.

O'Hara, M.J., 1968. The bearing of phase equilibria studies in synthetic and natural systems on the origin and evolution of basic and ultrabasic rocks. Earth-Sci. Rev. 4, 69–133.

Powell, R., Holland, T.J.B., Worley, B., 1998. Calculating phase diagrams involving solid solutions via non-linear equations, with examples using THERMOCALC. J. Metamorph. Geol. 16, 577–588.

Putirka, K.D., Perfit, M.R., Ryerson, F.J., Jackson, M.G., 2007. Ambient and excess mantle temperatures, olivine thermometry, and active vs. passive upwelling. Chem. Geol. 241 (3–4), 177–206.

Rudge, J.F., Maclennan, J., Stracke, A., 2013. The geochemical consequences of mixing melts from a heterogeneous mantle. Geochim. Cosmochim. Acta 114 (C), 112–143.

Salters, V.J.M., Stracke, A., 2004. Composition of the depleted mantle. Geochem. Geophys. Geosyst. 5 (5).

Shorttle, O., Maclennan, J., 2011. Compositional trends of Icelandic basalts: implications for short-length scale lithological heterogeneity in mantle plumes. Geochem. Geophys. Geosyst. 12 (11).

Shorttle, O., Maclennan, J., Lambart, S., 2014. Quantifying lithological variability in the mantle. Earth Planet. Sci. Lett. 395, 24–40.

Shorttle, O., Rudge, J.F., Maclennan, J., Rubin, K.H., 2016. A statistical description of concurrent mixing and crystallization during MORB differentiation: implications for trace element enrichment. J. Petrol. 57, 2127–2162.

Sobolev, A.V., Hofmann, A.W., Kuzmin, D.V., Yaxley, G.M., Arndt, N.T., Chung, S.-L., Danyushevsky, L.V., Elliott, T., Frey, F.A., Garcia, M.O., 2007. The amount of recycled crust in sources of mantle-derived melts. Science 316, 412–417.

Stixrude, L., Lithgow-Bertelloni, C., 2011. Thermodynamics of mantle minerals – II. Phase equilibria. Geophys. J. Int. 184 (3), 1180–1213.

Stracke, A., Bourdon, B., 2009. The importance of melt extraction for tracing mantle heterogeneity. Geochim. Cosmochim. Acta 73 (1), 218–238.

Tarantola, A., 2005. Inverse Problem Theory and Methods for Model Parameter Estimation. SIAM: Society for Industrial and Applied Mathematics, Philadelphia.

Walter, M.J., 1998. Melting of garnet peridotite and the origin of komatiite and depleted lithosphere. J. Petrol. 39 (1), 29–60.

Workman, R.K., Hart, S.R., 2005. Major and trace element composition of the depleted MORB mantle (DMM). Earth Planet. Sci. Lett. 231 (1), 53–72.